Earth and Planetary Science Letters 498 (2018) 362–376

Contents lists available at ScienceDirect

Earth and Planetary Science Letters

www.elsevier.com/locate/epsl

Constraining the evolution of Neogene ocean carbonate chemistry using the boron isotope pH proxy

S.M. Sosdian [a,*], R. Greenop [b,c], M.P. Hain [b,d], G.L. Foster [b], P.N. Pearson [a], C.H. Lear [a]

[a] Cardiff University, School of Earth & Ocean Sciences, Cardiff, CF10 3AT, UK
[b] Ocean and Earth Science, National Oceanography Centre Southampton, University of Southampton Waterfront Campus, Southampton, UK
[c] University of St. Andrews, School of Earth and Environmental Sciences, St. Andrews, UK
[d] Earth and Planetary Sciences, University of California, Santa Cruz, CA 95064, USA

ARTICLE INFO

Article history:
Received 3 May 2017
Received in revised form 11 June 2018
Accepted 13 June 2018
Available online 20 July 2018
Editor: H. Stoll

Keywords:
boron isotopes
foraminifera
carbonate system
Neogene
Miocene

ABSTRACT

Over the course of the Neogene, the Earth underwent profound climatic shifts from the sustained warmth of the middle Miocene to the development of Plio-Pleistocene glacial–interglacial cycles. Major perturbations in the global carbon cycle have occurred alongside these shifts, however the lack of long-term carbonate system reconstructions currently limits our understanding of the link between changes in CO_2, carbon cycling, and climate over this time interval. Here we reconstruct continuous surface ocean pH, CO_2, and surface ocean aragonite saturation state using boron isotopes from the planktonic foraminifer *Trilobatus trilobus* and we perform a sensitivity analysis of the key variables in our calculations (e.g. $\delta^{11}B_{sw}$, $[Ca]_{sw}$, CCD). We show that the choice of $\delta^{11}B_{sw}$ influences both seawater pH and CO_2 while $[Ca]_{sw}$ reconstructed dissolved inorganic carbon exerts a significant influence only on CO_2. Over the last 22 Myr, the lowest pH levels occurred in the Middle Miocene Climate Optimum (MMCO; 17–14 Myr ago) reaching $\sim 7.6 \pm 0.1$ units in all our scenarios. The extended warmth of the MMCO corresponds to mean CO_2 and aragonite saturation state levels of 470–630 ppm and 2.7–3.5, respectively. Despite a general correspondence between our CO_2 record and climate, all CO_2 scenarios show a peak at $\sim$9 Ma not matched by corresponding changes in climate reconstructions. This may suggest decoupling (i.e. significant CO_2 change without a discernible climate response) for a limited interval in the Late Miocene (11.6–8.5 Ma), although further refinement of our understanding of the temporal evolution of the boron isotopic composition of seawater is necessary to fully evaluate the nature of the relationship between CO_2 and climate. Nonetheless, from our long-term view it is clear that low-latitude open ocean marine ecosystems are unlikely to have experienced sustained surface pH and saturation levels below 7.7 and 1.7, respectively, during the past 14 million years (66% CI).

1. Introduction

Boron isotopes ($\delta^{11}B$) in marine carbonates have been exploited as a proxy for the marine carbonate system (i.e. pH, pCO_2) on multiple timescales within the Cenozoic (e.g. Sanyal et al., 1995; Palmer et al., 1998; Pearson and Palmer, 2000; Foster et al., 2012; Penman et al., 2013; Anagnostou et al., 2016; Gutjahr et al., 2017; Chalk et al., 2017). Plio-Pleistocene foraminiferal $\delta^{11}B$ derived reconstructions exhibit glacial–interglacial variability in pH and pCO_2, in good agreement with independent records (e.g. ice cores) (Seki et al., 2010; Bartoli et al., 2011; Hönisch et al., 2009; Henehan et al., 2013; Martínez-Botí et al., 2015a; Chalk et al., 2017). However, application of this proxy beyond the Plio-Pleistocene is not straightforward as calculation of pH and pCO_2 requires records of seawater chemistry (e.g. $\delta^{11}B_{sw}$, $[Ca]_{sw}$) and a second carbonate system parameter (e.g. total alkalinity (ALK), or dissolved inorganic carbon (DIC)) which currently have considerable uncertainties (Horita et al., 2002; Brennan et al., 2013; Pälike et al., 2012; Raitzsch and Hönisch, 2013; Greenop et al., 2017). Current reconstructions of the major ion composition of seawater, which impacts boron isotope reconstructions through influencing key dissociation constants and estimates of carbonate (CO_3^{2-}) concentration, rely on low-resolution fluid inclusion measurements (Horita et al., 2002; Brennan et al., 2013) and improved estimates await development of higher resolution records from a range of proxies. For the early Cenozoic, the likely upper and lower bounds of $\delta^{11}B_{sw}$ have been estimated using the $\delta^{11}B$-pH relationship, whilst estimates of the second carbonate system parameter

* Corresponding author.
E-mail address: SosdianS@cardiff.ac.uk (S.M. Sosdian).

https://doi.org/10.1016/j.epsl.2018.06.017

have been determined using Earth System modelling (Anagnostou et al., 2016; Gutjahr et al., 2017). According to Anagnostou et al. (2016), the early Eocene CO_2 concentration was 1400 ± 470 ppm decreasing to 550 ± 190 ppm in the early Oligocene. The uncertainty window on these estimates reflects uncertainty in calcite saturation and $\delta^{11}B_{sw}$ estimates, $\delta^{11}B_c$ measurement error, and possible atmosphere–ocean disequilibrium. Despite these relatively large uncertainties, it is clear that early Cenozoic pCO_2 was much higher than in the Plio-Pleistocene and CO_2 change was an important driver of climate change in the early Cenozoic. However, application of the $\delta^{11}B$-pCO_2 proxy during the more recent Neogene (2.6 to 23 Myrs ago) transition to a bipolar icehouse world is complicated by the fact that most reconstructions indicate a relatively dramatic shift in $\delta^{11}B_{sw}$ in the late Miocene to Pliocene. While there is first-order agreement between different records for the late Miocene $\delta^{11}B_{sw}$ rise, the exact timing, magnitude and rate of change of this shift remains uncertain (Pearson and Palmer, 2000; Lemarchand et al., 2002; Raitzsch and Hönisch, 2013; Greenop et al., 2017), with implications for the structure of $\delta^{11}B$-based reconstructions of pH and pCO_2 during the period. Furthermore, the history of carbonate chemistry (i.e. DIC and alkalinity) in this interval is poorly understood and currently is limited to model estimates that use pCO_2 estimates from GEOCARB carbon cycle models and/or paleo-pCO_2 proxy estimates paired with estimates of the calcite compensation depth (CCD) (Tyrrell and Zeebe, 2004; Ridgwell, 2005).

During the Neogene period, the Earth underwent profound changes from the warmth of the Middle Miocene Climatic Optimum (~14–17 Myrs ago; MMCO) to the expansion of the Antarctic ice sheet at 13.9 Ma (Lear et al., 2010). Dynamic changes in the carbon cycle have been proposed to be associated with these climatic shifts, involving changes in silicate weathering, volcanic emissions and the organic carbon subcycle (Derry and France-Lanord, 1996; France-Lanord and Derry, 1997; Raymo and Ruddiman, 1992; Raymo, 1994; Foster et al., 2012). The evolution of the carbonate system during this time interval therefore represents a critical gap in our understanding of climate–carbon cycle interactions. Previous CO_2 reconstructions derived from a disparate set of proxies (e.g. plant stomata, marine alkenones, paleosols, marine carbonate $\delta^{11}B$) have produced a wide range of estimates, yet with a general consensus that MMCO CO_2 levels were higher than preindustrial, and that CO_2 subsequently declined across the mid-Miocene climate transition (Kürschner et al., 2008; Foster et al., 2012; Zhang et al., 2013). Since CO_2 and pH are highly correlated variables in the ocean carbonate system, the discrepancies between existing CO_2 reconstructions (Pagani et al., 1999a, 1999b; Foster et al., 2012; Zhang et al., 2013) imply a lack in understanding of the ocean's history of pH change and the evolution of the carbon cycle and also, to some extent, an uncertainty in proxy systematics. Further, the degree of coupling between climate and CO_2 in the late Miocene is poorly constrained, limiting our ability to determine the importance of CO_2 variability in setting the evolution of Miocene climate (Pagani et al., 1999a, 1999b; LaRiviere et al., 2012). Thus, the lack of available records that constrain the ocean's carbonate chemistry is a critical impediment to establishing the relationship between the long-term Earth System evolution of carbon cycle and climate (Hönisch et al., 2012). Additionally, without detailed knowledge of long-term changes in seawater carbonate chemistry we are blind to its role in driving evolutionary adaptation and resilience of marine organisms to environmental change (Hönisch et al., 2012; Hain et al., 2015).

Here we use a new dataset of 40 planktic boron isotope measurements in conjunction with existing benthic data and new constraints on the evolution of seawater $\delta^{11}B$ (Lemarchand et al., 2002; Raitzsch and Hönisch, 2013; Greenop et al., 2017) to reconstruct surface pH and ocean carbon content for the past 22 million years. Combining our surface pH record with independent reconstructions of seawater calcium and magnesium concentrations, changes in the calcite compensation depth, deep-sea pH, and temperature, we calculate both atmospheric CO_2 and surface aragonite saturation state (Ω_{arag}). We also discuss the relative importance of the variable sources of uncertainty in these parameters on our reconstructions. With extensive uncertainty propagation using a Monte Carlo approach and sensitivity analysis we reconstruct long-term pH, aragonite saturation state and atmospheric CO_2 since the MMCO (0–17 Myrs ago). Our new record of ocean carbonate chemistry allows us to examine the role of CO_2 in the climate system over the course of the Neogene and contextualize future carbon emission pathways against this geological perspective.

2. Materials and methods

The boron isotope proxy relies on the principle that the ratio of the dominant boron species in seawater, borate ion and boric acid, varies as a function of pH (Dickson, 1990), which also controls the isotopic composition of the borate ion that is incorporated into a marine carbonate such as a planktic foraminiferal calcite (Vengosh et al., 1991; Hemming and Hanson, 1992; Foster and Rae, 2016). The foraminifer-derived pH record may then be used to estimate CO_2 levels and Ω_{arag} using assumptions about other carbonate system parameters. Early attempts at reconstructing pH and atmospheric CO_2 from fossil foraminifera over this interval (Spivack et al., 1993; Palmer et al., 1998; Pearson and Palmer, 2000) are qualitatively useful but have been superseded by a revised understanding of boron isotope systematics and analytical developments (see discussion in Seki et al., 2010; Foster et al., 2012; Anagnostou et al., 2016).

2.1. Sample locations and site details

In this study we analysed the $CaCO_3$ shells of a single planktic foraminifera species, *Trilobatus trilobus*. This species was formerly assigned to the genus *Globigerinoides* but is no longer considered part of that genus (Spezzaferri et al., 2015). The species is sometimes referred to as *T. sacculifer*, especially those individuals that bear a final sac-shaped final chamber, but the feature is ecophenotypic (André et al., 2013) and the name *trilobus* has priority. In this study we avoided individuals with sac-shaped chambers. Unusually for planktic foraminifera, *T. trilobus* displays no significant cryptic genetic diversity (André et al., 2013). It lives in the upper part of the water column in association with dinoflagellate photosymbionts, although it probably sinks towards the end of its life cycle at gametogenesis, somewhat complicating the shell chemistry (e.g. Birch et al., 2013). The species is widely used in boron isotope studies because it is one of the few to survive almost the entire Neogene and Quaternary periods (Spezzaferri et al., 2015) and a species-specific calibration for $\delta^{11}B$-pH exists (discussed further below; Sanyal et al., 2001; Seki et al., 2010; Foster et al., 2012; Greenop et al., 2014).

We analysed the $\delta^{11}B$ of 40 samples of this species from geographically diverse locations including Ocean Drilling Program (ODP) Site 926 ($n = 26$; western tropical North Atlantic), ODP Site 761 ($n = 3$; tropical Indian Ocean), ODP Site 872 ($n = 7$; tropical Pacific Ocean), and ODP Site 1000 ($n = 4$; Caribbean Sea). This dataset supplements previously published *T. trilobus* analyses from ODP site 668 (Hönisch et al., 2009), ODP Site 761 (Foster et al., 2012; Greenop et al., 2014), ODP Site 926 (Foster et al., 2012), ODP Site 999 (Bartoli et al., 2011; Seki et al., 2010; Caribbean Sea), ODP 1264 (Stap et al., 2016) and outcrops of the Blue Clay formation in Malta (Badger et al., 2013) and previously published *Globigeri-*

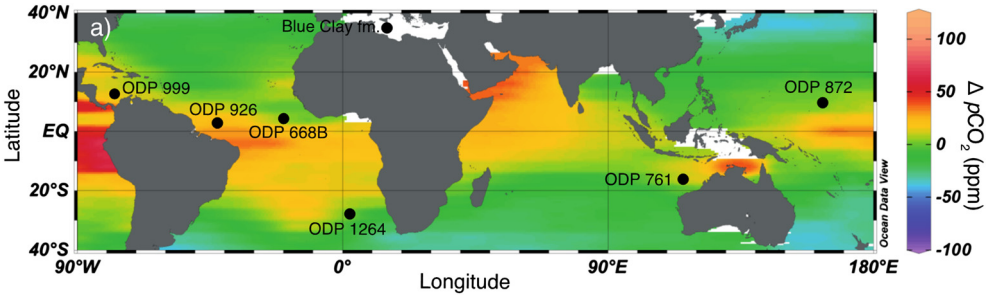

Fig. 1. Mean annual air–sea disequilibria with respect to pCO_2 (Takahashi et al., 2017) corrected for anthropogenic DIC invasion (Key et al., 2004) showing modern locations of ODP/DSDP sites used in this study (black circles). The modern extent of disequilibria at all sites is <25 ppm. Surface ocean disequilibria plot made using Ocean Data View (Schlitzer, 2012).

noides ruber analyses from ODP 999 (Martínez-Botí et al., 2015a; Chalk et al., 2017) (Fig. 1). Sea surface temperatures (SSTs) were reconstructed from these sites. ODP Site 761 (16°S, 115°E, 2179 m water depth) is situated in the Indian Ocean on the Wombat Plateau. ODP Site 926 (3°N, 42°W, 3598 m water depth) in the western equatorial Atlantic Ocean on Ceara Rise. ODP Site 872 (10°N, 162°E, 1287 m water depth) is in the tropical north Pacific gyre on the sedimentary caps of flat-topped seamounts. ODP Site 1000 (16°N, 79°W, 927 m water depth) is situated in the Caribbean Sea on the Nicaraguan Rise on a drowned carbonate platform.

Our sites are far removed from coastal influences and sources of upwelling, and likely remained close to equilibrium with atmospheric CO_2 and therefore variations in atmospheric CO_2 are likely the dominant control on $\delta^{11}B$ variability at all study sites (Pearson and Palmer, 2000; Takahashi et al., 2009, 2017; Hönisch et al., 2009; Bartoli et al., 2011; Seki et al., 2010; Foster et al., 2012; Badger et al., 2013; Greenop et al., 2014; Martínez-Botí et al., 2015a; Chalk et al., 2017) (Fig. 1). Although foraminifer shells from these sites (except Malta) exhibit the recrystallized textures common in deep sea pelagic sites (e.g. Sexton et al., 2006), existing evidence suggests that the boron isotopic signal remains intact within the foraminifer test during recrystallisation, hence the process does not strongly affect $\delta^{11}B$ (Foster et al., 2012; Badger et al., 2013; Edgar et al., 2015).

2.2. Age model

Our age model for ODP Site 761 uses biostratigraphic datums (Holbourn et al., 2004) on the CK95 timescale (Cande and Kent, 1995; Supplementary Table S1). The age model for ODP Site 926 is a polynomial fit through nannofossil and planktic foraminifer biostratigraphic datums based on the shipboard report (Site 926 Shipboard Scientific Party, 1995) and post-cruise refinement (Chaisson and Pearson, 1997; Pearson and Chaisson, 1997) adapted to the CK95 timescale. Ages for ODP Site 872 was calculated by linear interpolation between reliable biostratigraphic datums (Pearson, 1995) from the early to mid-Miocene. Note that for ODP Site 872, age estimates for sample depths 105.71 and 106.79 mbsf have large uncertainty (±1 Ma) as evidence for reworking is present in this section, however this is not significant at the resolution of this study for the early Miocene. Nannofossil and planktic foraminifer biostratigraphic datums tied to the CK95 timescale were used for the age model at ODP Site 1000A (Site 1000 Shipboard Scientific Party, 1997a, 1997b). The age models from published boron isotope records from ODP Sites 761 (Foster et al., 2012; Greenop et al., 2014), 926 (Foster et al., 2012), and the Blue Clay Formation (Badger et al., 2013) were put on the CK95 timescale in a similar manner using shipboard reports, published biostratigraphic datums (Holbourn et al., 2004; Site 926 Shipboard Scientific Party, 1995; Site 999 Shipboard Scientific Party, 1997a, 1997b; Hilgen et al., 2009). Previously published records from the Plio-Pleistocene (<5 Myr) (Hönisch et al., 2009; Seki et al., 2010; Bartoli et al., 2011; Martínez-Botí et al., 2015a; Stap et al., 2016; Chalk et al., 2017) are on their original orbitally tied age models.

2.3. Analytical methodology

Between 100 and 150 shells of *T. trilobus* were picked from the 300–355 µm size fraction and cleaned following the oxidative cleaning method (Barker et al., 2003). Samples were dissolved in 0.5M HNO_3 and stored for boron isotope analysis in Teflon vials. Following Foster (2008) and as detailed in Foster et al. (2013), boron separation from the calcium matrix was performed using the boron specific resin Amberlite IRA 743. Boron isotope analysis was performed on a Thermo-Fisher Scientific Neptune multi collector inductively coupled plasma mass spectrometer (MC-ICPMS) at the University of Southampton with a sample-standard bracketing routine (Foster et al., 2013; Henehan et al., 2013).

External reproducibility is calculated following Rae et al. (2011) as follows:

$$2\sigma = 2.25\exp^{-23.01[^{11}B]} + 0.28\exp^{-0.64[^{11}B]} \quad (1)$$

$$2\sigma = 33450\exp^{-168.2[^{11}B]} + 0.311\exp^{-1.477[^{11}B]} \quad (2)$$

where $[^{11}B]$ is the intensity of ^{11}B signal in volts and equation (1) and equation (2) used with 10^{-11} and 10^{-12} resistors, respectively ($\delta^{11}B_{planktic}$ $2\sigma \pm 0.22$–$1.00‰$). In house standards (JCP-1; Hathorne et al., 2013) were processed with each column batch ($n = 4$) and these and boric acid standards repeatedly analysed during each analytical session were consistent with the long-term reproducibility (Supplementary Table S2).

Calibration studies have shown that the borate species is predominantly incorporated in the calcium carbonate shell and thus the boron isotopic composition of borate can be used to estimate ocean pH (Vengosh et al., 1991; Hemming and Hanson, 1992; Sanyal et al., 2001). To calculate pH from the $\delta^{11}B$ of *T. trilobus* we account for the species-specific offset between $\delta^{11}B_{borate}$ in seawater and $\delta^{11}B$ of the foraminiferal calcite due to vital effects (equation (3)) (Foster and Rae, 2016; Henehan et al., 2016). We use the calibration slope from Sanyal et al. (2001) calculated following Martínez-Botí et al. (2015b) with the intercept based on core-top $\delta^{11}B$ *T. sacculifer* 300–355 µm data from Seki et al. (2010) with estimates of surface water borate from Henehan et al. (2016):

$$\delta^{11}B_{borate} = \left(\delta^{11}B_{T.trilobus} - 2.69\right)/0.833 \quad (3)$$

This species-specific calibration curve is used to estimate the $\delta^{11}B$ of borate ion. The measurement uncertainty of $\delta^{11}B_{trilobus}$ estimated by the external reproducibility is fully propagated with an appropriately scaled normal distribution.

Here we compile our *T. trilobus* $\delta^{11}B$ data with previously published $\delta^{11}B$ records from the Miocene (Foster et al., 2012; Badger et al., 2013; Greenop et al., 2014) and Plio-Pleistocene (Fig. 2B; Hönisch et al., 2009; Bartoli et al., 2011; Seki et al., 2010; Martínez-Botí et al., 2015a; Stap et al., 2016; Chalk et al., 2017). To estimate $\delta^{11}B_{borate}$ and surface ocean pH, we applied size-fraction and species-specific $\delta^{11}B_{borate}$–$\delta^{11}B$ calibrations (Supplementary Table S3). As previously published $\delta^{11}B$ analyses in this compilation were performed using a range of techniques, we apply inter-instruments offsets to the published negative thermal ionization mass spectrometry (N-TIMS) data to correct to the MC-ICPMS and in doing so account for the well-documented instrument dependent offset in these NTIMS data (Foster et al., 2013; Farmer et al., 2016) due to differences in chemical composition of sample (i.e. B/Ca) and other reasons that are currently unclear (Farmer et al., 2016). Some $\delta^{11}B$ data from Hönisch et al. (2009) were performed on two different TIMS, the NBS design instrument at Stony Brook and Thermo Scientific Triton at LDEO. To account for this and correct the data to the MC-ICPMS, we use an offset of −1.1‰, as determined from an interlaboratory comparison of five modern and fossil samples measured on both the NBS design and Triton NTIMS (Hönisch et al., 2009). To align the $\delta^{11}B$ datasets collected on the Triton (Hönisch et al., 2009; Bartoli et al., 2011; Stap et al., 2016) with the Neptune MC-ICPMS used here, we adopt the −1.12‰, offset presented in Farmer et al. (2016) based on average of 5 fossil samples measured on both the Triton NTIMS and Neptune (Supplementary Fig. S1). Using this approach, the degree of the $\delta^{11}B_{borate}$ overlap between datasets from both instruments is still relatively poor in the region 2.5–3.0 Ma. To overcome this, we estimate pH and then tune the NTIMS offsets for overlapping pH datasets until there is a good agreement between NTIMS and MC-ICPMS. The best fit is achieved when we apply an additional −1.0‰ offset to the Triton planktic $\delta^{11}B$ datasets. This additional offset suggests that further work is needed to provide a mechanistic understanding of the offset between MC-ICPMS and NTIMS techniques. We do not include the dataset of Stap et al. (2016) in the compilation as even with this treatment of the NTIMS offset the $\delta^{11}B_{borate}$ values exhibit substantial scatter and do not align with any of the other records (Supplementary Fig. S1). We applied no offsets to the benthic $\delta^{11}B$ data from Greenop et al. (2017) and Raitzsch and Hönisch (2013), measured on the MC-ICPMS and NTIMS, respectively, as the data agree well in their raw state (see Greenop et al., 2017).

Tandem trace element analyses were performed on a small aliquot (<10%) of each sample measured here on the Thermo-Fisher Scientific Element 2 single collector inductively coupled plasma mass spectrometer at University of Southampton following the method outlined in Henehan et al. (2013). Over the duration of this study, analytical reproducibility for Mg/Ca was ±2.7% (2σ). *T. trilobus* Mg/Ca values were converted to sea surface temperatures (SST) using the calibration of Anand et al. (2003) with a correction for seawater Mg/Ca (Horita et al., 2002; Brennan et al., 2013) following Hasiuk and Lohmann (2010) using a power constant of 0.41 (Delaney et al., 1985; Evans and Mueller, 2012) (Fig. 2C; Supple-

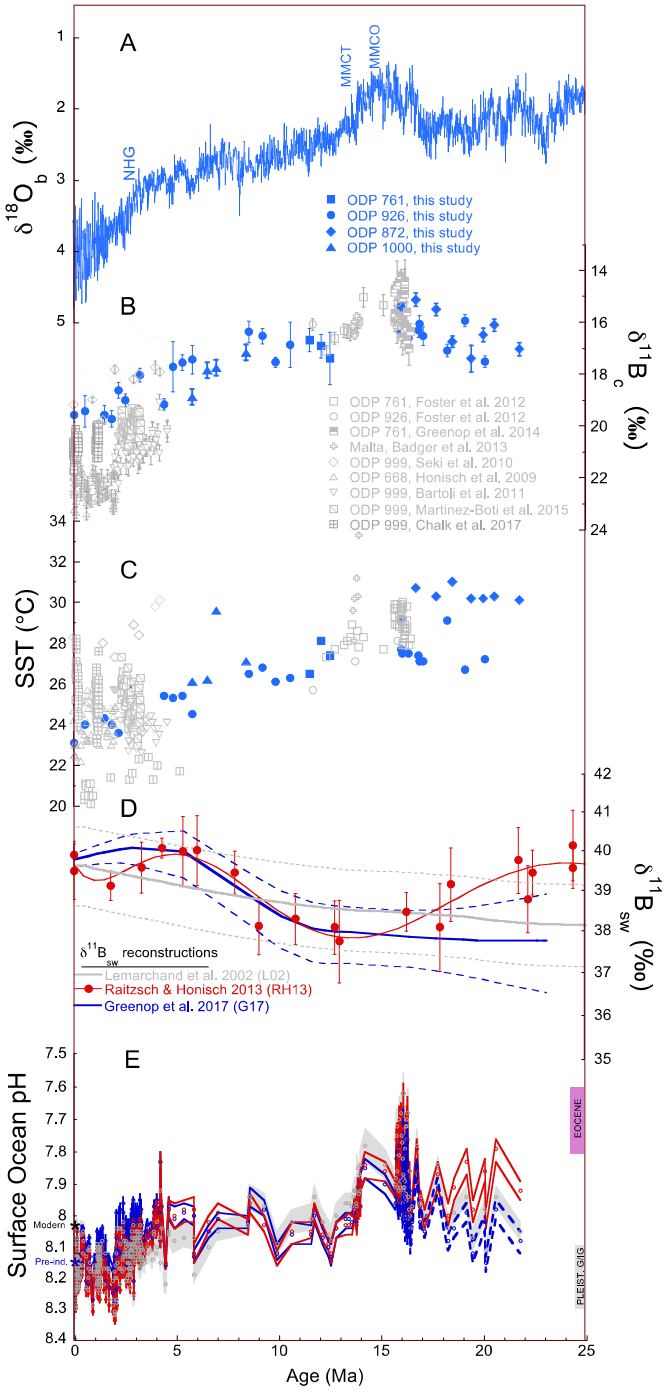

Fig. 2. (A) Benthic foraminiferal oxygen isotope ($\delta^{18}O$) record reflecting changes in global climate (Zachos et al., 2008); Labels indicate the timing of the Middle Miocene Climate Optimum (MMCO), Middle Miocene Climate Transition (MMCT), and Northern Hemisphere Glaciation (NHG); (B) Boron isotopic composition ($\delta^{11}B$) of planktonic foraminifer *T. trilobus* (300–355 μm) record from this study (blue) and published data from *T. trilobus* and *G. ruber* (Hönisch et al., 2009; Seki et al., 2010; Bartoli et al., 2011; Foster et al., 2012; Badger et al., 2013; Greenop et al., 2014; Martínez-Botí et al., 2015a; Chalk et al., 2017) (grey). Note the inverted axis with low $\delta^{11}B$ corresponding to low pH and pCO_2. Error bars denote analytical external reproducibility (2 s.d.); (C) Sea surface temperatures (SSTs) derived from foraminiferal Mg/Ca from this study (blue) and published SST data derived from Mg/Ca (Hönisch et al., 2009; Bartoli et al., 2011; Foster et al., 2012; Badger et al., 2013; Greenop et al., 2014; Martínez-Botí et al., 2015a; Stap et al., 2016; Chalk et al., 2017) and alkenone U^k37 values (Seki et al., 2010) (grey). Sites are coloured as in (B). (D) $\delta^{11}B_{sw}$ reconstructions from Lemarchand et al. (2002) with ±1‰ confidence interval, Raitzsch and Hönisch (2013) using the fractionation factor of Klochko et al. (2006) and 2 sigma uncertainty, and Greenop et al. (2017) with 95% confidence intervals. These reconstructions are referred to hereafter as "$\delta^{11}B_{sw}$-L02", "$\delta^{11}B_{sw}$-RH13", and "$\delta^{11}B_{sw}$-G17". (E) Surface ocean pH reconstructions using the three $\delta^{11}B_{sw}$ reconstructions in (D). Note there is an additional $\delta^{11}B_{sw}$ 'RH13' reconstruction presented in Raitzsch and Hönisch (2013) not shown here calculated using an apparent fractionation factor. Here we use the Klochko et al. (2006) derived $\delta^{11}B_{sw}$ value to be consistent with the $\delta^{11}B$ calculations in this study. 66% confidence intervals are plotted. Dashed lines represent $\delta^{11}B_{sw}$-G17 estimates from >17 Ma to highlight uncertainties associated with the $\delta^{11}B_{sw}$ reconstruction. Pre-industrial and 2017 levels are highlighted by blue and black asterisks respectively on the pH axis. Pleistocene and Eocene pH estimates are shown as vertical bars on the right side of panel E (Hönisch et al., 2009; Foster, 2008; Anagnostou et al., 2016). (For interpretation of the colours in the figure(s), the reader is referred to the web version of this article.)

mentary Fig. S2). SST estimates were calculated in a similar manner for previously published Mg/Ca records (Hönisch et al., 2009; Seki et al., 2010; Bartoli et al., 2011; Foster et al., 2012; Badger et al., 2013; Greenop et al., 2014; Martínez-Botí et al., 2015a; Chalk et al., 2017). The following equations were used to correct for Mg/Ca seawater and estimate temperature (in units of °C) from foraminiferal Mg/Ca (Mg/Ca_{test}):

$$T(^{\circ}C) = \ln\left(\frac{[Mg/Ca]_{foram}}{0.38[Mg/Ca]_{sw.c}}\right)/0.09 \quad (4)$$

$$[Mg/Ca]_{sw.c} = \left(\frac{[Mg/Ca]_{sw.a}}{[Mg/Ca]_{sw.m}}\right)^{0.41} \quad (5)$$

where equation (4) is the generic planktic foraminifera calibration of Anand et al. (2003) with a correction applied to the seawater Mg/Ca ratio to account for past Mg/Ca changes. This correction, given in equation (5), requires the seawater Mg/Ca for the age of the sample ($[Mg/Ca]_{sw.a}$) and modern seawater Mg/Ca for which the calibration was established ($[Mg/Ca]_{sw.m}$) to yield the corrected ratio for the paleotemperature equation $[Mg/Ca]_{sw.c}$. Trace element data were also used to check for foraminiferal cleaning efficiency (Barker et al., 2003). In all cases Al/Ca was <100 µmol/mol and in the majority of cases Mn/Ca was <1000 µmol/mol indicating cleaning was efficient. Some Mn/Ca values were higher than our 1000 µmol/mol threshold, for example at ODP site 926, but in all cases they do not covary with Mg/Ca or $\delta^{11}B$ (Supplementary Fig. S3). The ODP site 761 Mg/Ca presented in this study is of too low resolution to judge the influence of contamination through correlation of Mg/Ca and Mn/Ca so instead we look to benthic foraminiferal Mg/Ca data from the same site which shows a lack of correlation between Mn/Ca and Mg/Ca (see Lear et al., 2015 for further discussion). ODP site 872 shows no positive correlation between Mn/Ca and Mg/Ca.

2.4. Solving for pH and the carbonate system

To convert our reconstruction of surface $\delta^{11}B_{borate}$ into pH, CO_2 and carbonate saturation state requires three steps: (1) calculate the acid/base chemistry equilibrium constants based on independently known temperature, salinity and seawater major ion composition; (2) calculate surface water pH using the appropriate equilibrium constants, reconstructed $\delta^{11}B_{borate}$ and independently estimated seawater $\delta^{11}B$; and (3) calculate surface water carbonate chemistry based on reconstructed pH and an independently known carbonate system parameter. The uncertainties associated with the various input parameters need to be propagated through the full set of calculations. The input parameters are presented in Fig. 3 and below we describe these calculations in more detail.

All required acid/base chemistry equilibrium constants, including the boric acid dissociation constant pK_B^*, are calculated using the MyAMI model (Hain et al., 2015) based on reconstructed SST, sea surface salinity (SSS), water depth, and seawater major ion composition. We note that the calcium-to-bicarbonate interaction coefficient $\beta^{(0,1)}_{Ca\text{-}HCO_3}$ used in MyAMI was updated from Harvie et al. (1984; $\beta^{(0)}_{Ca\text{-}HCO_3} = 0.4$ and $\beta^{(1)}_{Ca\text{-}HCO_3} = 2.977$, see their Table 1) to He and Morse (1993; $\beta^{(0)}_{Ca\text{-}HCO_3} = 0.2$ and $\beta^{(1)}_{Ca\text{-}HCO_3} = 0.3$, see their Table 5) to bring MyAMI into agreement with experimental data of Pytkowicz and Hawley (1974). SST estimates are derived from Mg/Ca ratios from *T. trilobus* for ODP Sites 761, 926, 872, 1000A, and Malta from this study and previously published records (Foster et al., 2012; Badger et al., 2013; Greenop et al., 2014). SST estimates for ODP Site 999 (Seki et al., 2010) are based on a published record derived from the $U^{K'}_{37}$ proxy. In our CO_2 calculations we assign an uncertainty in SST of ±1 °C (1σ), which is propagated into

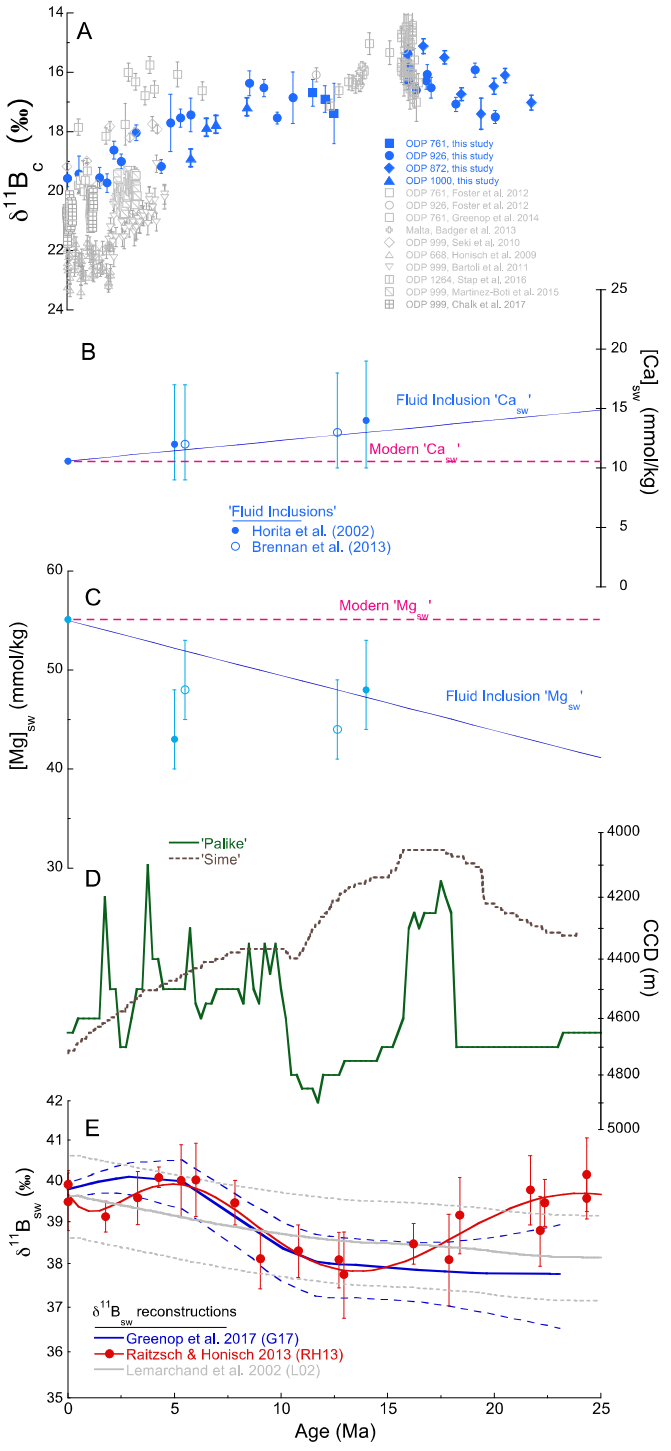

Fig. 3. Input variables for the sensitivity analysis including compiled (A) planktic $\delta^{11}B_{borate}$ estimated after offsets were applied to align planktic $\delta^{11}B_{calcite}$ performed using the NTIMS (grey; Hönisch et al., 2009; Bartoli et al., 2011) and MC-ICPMS (blue; Seki et al., 2010; Foster et al., 2012; Badger et al., 2013; Greenop et al., 2014; Martínez-Botí et al., 2015a; Chalk et al., 2017) techniques; (B) fluid inclusion based seawater [Ca^{2+}] and (C) [Mg^{2+}] estimates (Horita et al., 2002; Brennan et al., 2013), (D) CCD reconstructions (Sime et al., 2007; Pälike et al., 2012), and (E) three $\delta^{11}B_{sw}$ reconstructions (L02, RH13, G17; Lemarchand et al., 2002; Raitzsch and Hönisch, 2013; Greenop et al., 2017). Note there is an additional $\delta^{11}B_{sw}$ 'RH13' reconstruction presented in Raitzsch and Hönisch (2013) not shown here calculated using an apparent fractionation factor. Here we use the Klochko et al. (2006) derived $\delta^{11}B_{sw}$ value to be consistent with the $\delta^{11}B$ calculations in this study.

these calculations. Salinity has minimal influence on pH calculations (±1 psu = ±0.006 pH units) and thus we assume modern salinity at each site, estimated from nearby GLODAP stations (Key et al., 2004), with an uncertainty of ±1 psu (1σ). The MyAMI calculated conditional equilibrium constants used for carbon chemistry calculations account for secular seawater [Ca^{2+}] and [Mg^{2+}] changes. As further described in section 3.2 below, we carry out all calculations for two distinct [Ca^{2+}] and [Mg^{2+}] scenarios: (a) constant modern seawater major ion composition, and (b) seawater [Ca^{2+}] and [Mg^{2+}] changing with time according to the reconstructions of Horita et al. (2002) and Brennan et al. (2013). In both seawater major ion scenarios we attach a nominal uncertainty of 2.25 mmol/kg (1σ) to both [Ca^{2+}] and [Mg^{2+}].

To calculate surface pH from our boron isotope data we follow previous work (e.g., Vengosh et al., 1991; Foster and Rae, 2016) using eqns. (6) and (7):

$$\delta^{11}B = \left\lfloor \left(\frac{^{11}B/^{10}B_{sample}}{^{11}B/^{10}B_{NIST951}} \right) - 1 \right\rfloor \times 1000 \quad (6)$$

$$pH = pK_B^* - \log\left(-\frac{\delta^{11}B_{SW} - \delta^{11}B_{borate}}{\delta^{11}B_{SW} - (\alpha_B \times \delta^{11}B_{borate}) - 1000 \times (\alpha_B - 1)} \right) \quad (7)$$

where $\delta^{11}B$ is the ratio of ^{10}B and ^{11}B expressed in delta notation (in per mil, ‰), $^{11}B/^{10}B_{NIST951}$ is the isotopic ratio of the NIST SRM 951 boric acid standard ($^{11}B/^{10}B$ = 4.04367) (Catanzaro et al., 1970). The boric acid dissociation constant pK_B^* is calculated as described above. The boron isotope fractionation factor α_B is taken to be 1.0272 (Klochko et al., 2006). The isotopic composition of borate, $\delta^{11}B_{borate}$, is based on our *T. trilobus* data and calibration equation (3) and previously published planktic $\delta^{11}B$ data and specified calibration equations (Supplementary Table S3). As further described in section 3.2 below, we carry out all calculations for three distinct scenarios for secular change in seawater boron isotopic composition ($\delta^{11}B_{sw}$) using the reconstructions by (a) Lemarchand et al. (2002) ("L02"), (b) Raitzsch and Hönisch (2013) ("RH13") and (c) Greenop et al. (2017) ("G17"). Each record is used with its respective reported uncertainty assuming normal distribution.

To calculate CO_2 and carbonate saturation state (Ω_{CaCO_3}) from our pH reconstruction requires independent knowledge of ambient dissolved inorganic carbon concentration DIC, or any other carbonate system parameter:

$$CO_2 = \frac{DIC}{K_0^*} * \frac{[H^+]^2}{[H^+]^2 + [H^+]K_1^* + K_1^*K_2^*} \quad (8a)$$

$$\Omega_{CaCO_3} = \frac{[Ca^{2+}] * DIC}{K_{CaCO_3}^*} * \frac{K_1^*K_2^*}{[H^+]^2 + [H^+]K_1^* + K_1^*K_2^*} \quad (8b)$$

The different K^* terms represent the equilibrium constants governing carbonate chemistry, which we can calculate using the MyAMI model as described above. The [Ca^{2+}] concentration is internally consistent with the MyAMI calculations for both seawater major ion composition scenarios described above (i.e., constant modern or based on Horita et al., 2002 and Brennan et al., 2013).

The dissolved inorganic carbon concentration of seawater, DIC, is not generally known through Earth history, and given residence time constraints it may have experienced long-term changes over our study interval (Ridgwell, 2005). As estimating past DIC change in detail is beyond the scope of this study here we devise a data-driven approach to account, to the first order, for long-term drift in DIC in lieu of simply presuming constant DIC across the study interval. To this end we use published benthic foraminiferal $\delta^{11}B$ data (Raitzsch and Hönisch, 2013; Greenop et al., 2017) to generate a deep ocean pH record using equation (7), using the same three scenarios for $\delta^{11}B_{sw}$ (i.e. L02, RH13, G17) that we also use to generate our surface ocean pH records (Lemarchand et al., 2002; Raitzsch and Hönisch, 2013; Greenop et al., 2017). We then combine deep ocean pH with estimates of deep ocean carbonate ion concentration ([CO_3^{2-}]) to solve for deep ocean DIC. Deep ocean [CO_3^{2-}] is calculated based on past changes in the CCD (using Sime et al., 2007 and Pälike et al., 2012 as two scenarios) in conjunction with the [Ca^{2+}] defined by the two scenarios for seawater major ion changes (i.e., constant modern seawater composition versus trends based on data by Horita et al., 2002 and Brennan et al., 2013). We define deep ocean carbonate ion concentration as:

$$[CO_3^{2-}]_{deep} = \frac{K_{CaCO_3}^* * \Omega_{calcite}}{[Ca^{2+}]} \quad (9)$$

where $K_{CaCO_3}^*$ is calculated using the MyAMI model for the hydrostatic pressure at the reconstructed depth of the CCD and the calcite saturation index $\Omega_{calcite}$ assumes a nominal value of 1. Hence, the implications of past changes in the CCD for carbonate chemistry are represented via the strong pressure dependence of $K_{CaCO_3}^*$, which increases by ~16% per kilometre water depth. We then combine deep ocean carbonate ion concentration and the benthic foraminifera-based pH record to yield estimated DIC:

$$DIC = \frac{[H^+]^2 + [H^+]K_1^* + K_1^*K_2^*}{K_1^*K_2^*} * [CO_3^{2-}]_{deep} \quad (10)$$

Our data-driven approach makes the assumption that there is no difference in the carbonate ion concentration between the CCD and the core sites of the deep ocean pH reconstruction. This treatment is a significant simplification and certain to introduce error in the DIC estimate. However, we note that observed modern ocean deep ocean gradients in carbonate chemistry are relatively small when compared for example to the depth dependence of $K_{CaCO_3}^*$ that we include to represent past CCD changes. Furthermore, by assuming a nominal $\Omega_{calcite}$ of 1 at the pressure of the CCD we effectively introduce systematic bias towards greater estimated DIC because bottom waters at the CCD exhibit moderate undersaturation ($\Omega < 1$) so as to facilitate the near complete dissolution of calcite on the seafloor. With these caveats in mind we note that under all scenarios the DIC estimated from the youngest data is lower than deep ocean DIC in the modern ocean (Supplementary Fig. 4), in particular in the scenarios based on the $\delta^{11}B_{sw}$ record of Raitzsch and Hönisch (2013). Therefore, we caution that the approach taken here to estimate DIC appears to be biased towards lower absolute values by about 10–20% depending on scenario. However, as is evident from the comparison of the different sensitivity scenarios, the change in estimated DIC over the course of the Neogene is dominantly driven by the counteracting effects of secular [Ca^{2+}] decline and the tendency of deep ocean pH to increase, which act to raise and lower estimated DIC, respectively.

While our approach to estimating past DIC has unaccounted bias, the first-order changes in the DIC estimates over time can be attributed to trends in the data-driven input parameters and is reasonable first approach. Therefore, we carry out linear regression on the output of a 10,000 member Monte-Carlo simulation of the deep ocean input data, extracting for each scenario the estimated DIC rate of change and the intercept uncertainty. Based on these regression results, we estimate surface ocean DIC change relative to its known modern concentration for each respective scenario of $\delta^{11}B_{sw}$, CCD and seawater major ion composition. That is, we set

surface DIC to its modern reference value of 2000 µmol/kg plus the regressed change over time plus a nominal uncertainty based on the regression intercept value (Supplementary Fig. S5) (i.e., 1σ of 190 to 270 µmol/kg depending on scenario; see Supplementary Table S4 for regression results). We note that in the early Miocene interval (>17 Myr) of the Greenop et al. (2017) $\delta^{11}B_{sw}$ reconstruction large uncertainties exist in the $\delta^{11}B_{sw}$ value for the oldest samples which cause an edge effect in the smoothing algorithm used in that study (Greenop et al., 2017). Thus, for the regressions using the Greenop et al. (2017) $\delta^{11}B_{sw}$ scenario we only use benthic $\delta^{11}B$ data <16 Ma to regress DIC and extrapolated further back in time. This is necessary because this possible bias would have been propagated into the regression of DIC change, thus affecting our reconstruction for the entire record.

We note that applying the DIC change regressed from the benthic data to the surface we implicitly assume a constant DIC gradient (ΔDIC). An alternative would be to regress deep alkalinity and assume a constant alkalinity gradient (ΔALK) instead, but we find that these two alternative approaches yield nearly identical results (see Supplementary Fig. S6). We argue that the surface pH that we reconstruct is the dominant driver of reconstructed pCO_2 and surface carbonate saturation because it is a strong constraint on the ΔALK-to-ΔDIC difference. Whether ΔDIC or ΔALK are assumed to be constant therefore makes only a minimal difference for our purpose, and the deviation between these two assumptions falls well within the range of our propagated uncertainties.

DIC estimates vary between $\delta^{11}B_{sw}$ scenarios across the Neogene: both L02 and G17 show a long-term DIC rise (+20 to +37 µmol/kg per million years, depending on scenario, Supplementary Table S5) in contrast to RH13 scenario, which results in essentially constant DIC (+3 to +11 µmol/kg per million years, depending on CCD scenario, Supplementary Table S5) throughout the study period. That is, the scenarios based on the three available $\delta^{11}B_{sw}$ reconstructions collectively support a modest rate of long-term DIC increase over the study period, which integrated over the duration of the Neogene could amount to a significant expansion of the active carbon pool of the climate system. Along these lines, our assertion of significant Neogene DIC pool expansion agrees with the previously published model results from Tyrrell and Zeebe (2004), Ridgwell (2005), and Caves et al. (2016) (Supplementary Fig. S7).

The approach taken here is similar to Foster et al. (2012) which used a simple model anchored by paleo-pH depth profile and CCD reconstructions to estimate surface alkalinity and calculate pH and pCO_2. Using this approach, Foster et al. (2012) estimate surface alkalinity at 1293 ± 200 umol/kg at a single data point (12.72 Ma) and extrapolate across the mid-Miocene. The resultant average mid-Miocene DIC $\sim 1100 \pm 180$ umol/kg are much lower than estimates derived in this study (Supplementary Fig. S7). Building on this, Greenop et al. (2014) adopted the approach of Foster et al. (2012) but increased the uncertainty to $\pm$300 umol/kg to account for likely rapid CCD changes not resolved in available CCD reconstructions. Based on our new data-driven analysis and existing model based estimates (Ridgwell, 2005; Tyrrell and Zeebe, 2004) we argue that the approach by Foster et al. (2012) yielded DIC that was too low. Consequently, due to the higher DIC estimates applied here, the Mid-Miocene pCO_2 estimates calculated from planktic $\delta^{11}B$ data of Foster et al. (2012) and Greenop et al. (2014), as well as from our new data from ODP site 761 and 926, are significantly higher than previously published. While highlighting again the caveats in our estimates of surface DIC we argue that this approach is an improvement in deriving long-term DIC change for the boron isotope-based reconstruction of pCO_2 and carbonate saturation across the Neogene.

3. Results and discussion

3.1. $\delta^{11}B$ record of *T. trilobus* from the Neogene

Our $\delta^{11}B$ record displays a long-term trend in which low $\delta^{11}B$ is associated with high Mg/Ca in the same planktic foraminifera, and with low benthic oxygen isotope ratios ($\delta^{18}O$). All else being equal, this suggests that low pH (and thus high CO_2) is associated with high sea surface temperatures and some combination of relatively warm bottom waters and/or low global ice volume (Fig. 2). Reasonable agreement between $\delta^{11}B$ from geographically diverse sites suggests the record mainly reflects global carbon cycle variations rather than complications relating to diagenesis and variations in the extent of surface water (dis)equilibrium with respect to atmospheric CO_2 (Fig. 1). The broad correlations evident in Fig. 2 alone suggest a tight coupling between the carbon cycle (that predominantly drives $\delta^{11}B_c$ change) and climate (that predominantly drives $\delta^{18}O_b$ change) through the Neogene. Our new $\delta^{11}B$ data presented in this study shows similar variability to previously published $\delta^{11}B$ records from the Miocene (Foster et al., 2012; Badger et al., 2013; Greenop et al., 2014) and Plio-Pleistocene (Hönisch et al., 2009; Seki et al., 2010; Bartoli et al., 2011; Martínez-Botí et al., 2015a; Chalk et al., 2017) and fills in data gaps in the early Miocene and late Miocene (Fig. 2; Supplementary Fig. S1). From here on we compile $\delta^{11}B$ estimates from this study alongside previously published $\delta^{11}B$ records (with appropriate analytical offsets as required, see above) and calculate carbonate system variables to examine Neogene changes in the carbon cycle.

3.2. Scenarios and sensitivity testing

The calculations carried out in order to reconstruct seawater carbonate chemistry and atmospheric CO_2 require independent knowledge of the histories of seawater boron isotope composition ($\delta^{11}B_{sw}$) and major ion composition (especially $[Ca^{2+}]$ and $[Mg^{2+}]$) as well as the CCD. For each of these parameters we make at least two different choices and carry out the full set of calculations, including Monte-Carlo uncertainty propagation, for all twelve combinations. In this section we describe all scenarios and explain the agreements/disagreements between them. The output data for all scenarios is provided as a tabulated dataset in the supplemental material (Supplementary Table S6). In the section below, we show that the uncertainties in our reconstructions are dominated by the $\delta^{11}B_{sw}$ reconstructions, not the CCD, and hence only consider these scenarios in our main discussion (see section 3.3).

For our consideration of changes in $\delta^{11}B_{sw}$, we use the $\delta^{11}B_{sw}$ reconstructions of Lemarchand et al. (2002) ("L02"), Raitzsch and Hönisch (2013) ("RH13"), and Greenop et al. (2017) ("G17") (Fig. 2D). Specifically, RH13 uses benthic $\delta^{11}B$ and assumptions about deep ocean pH, G17 uses pH gradients in the ocean derived from planktic and benthic $\delta^{13}C$, whereas L02 is based on geochemical modelling of boron fluxes. Overall, all three records show a general increase through time from the middle Miocene to present, however, the $\delta^{11}B_{sw}$ records diverge in the early Miocene and late Miocene (Greenop et al., 2017; Fig. 2D). The divergence in the early Miocene (>17 Myr) and late Miocene amongst the three $\delta^{11}B_{sw}$ scenarios yields divergent pH and pCO_2 reconstructions for these time intervals but has only minor impact on our reconstruction of surface Ω_{arag} (Fig. 4). The G17 reconstruction has likely too low $\delta^{11}B_{sw}$ before 17 Myr due an edge effect (Greenop et al., 2017) and thereby yields anomalously high pH and low pCO_2 for this interval. Conversely, the RH13 reconstruction agrees well with the G17 record from the middle Miocene to present but is likely too high in the early Miocene as these authors assume a linear increase in surface pH through time (Fig. 2D). Further, because Raitzsch and Hönisch (2013) presuppose knowledge of pH in

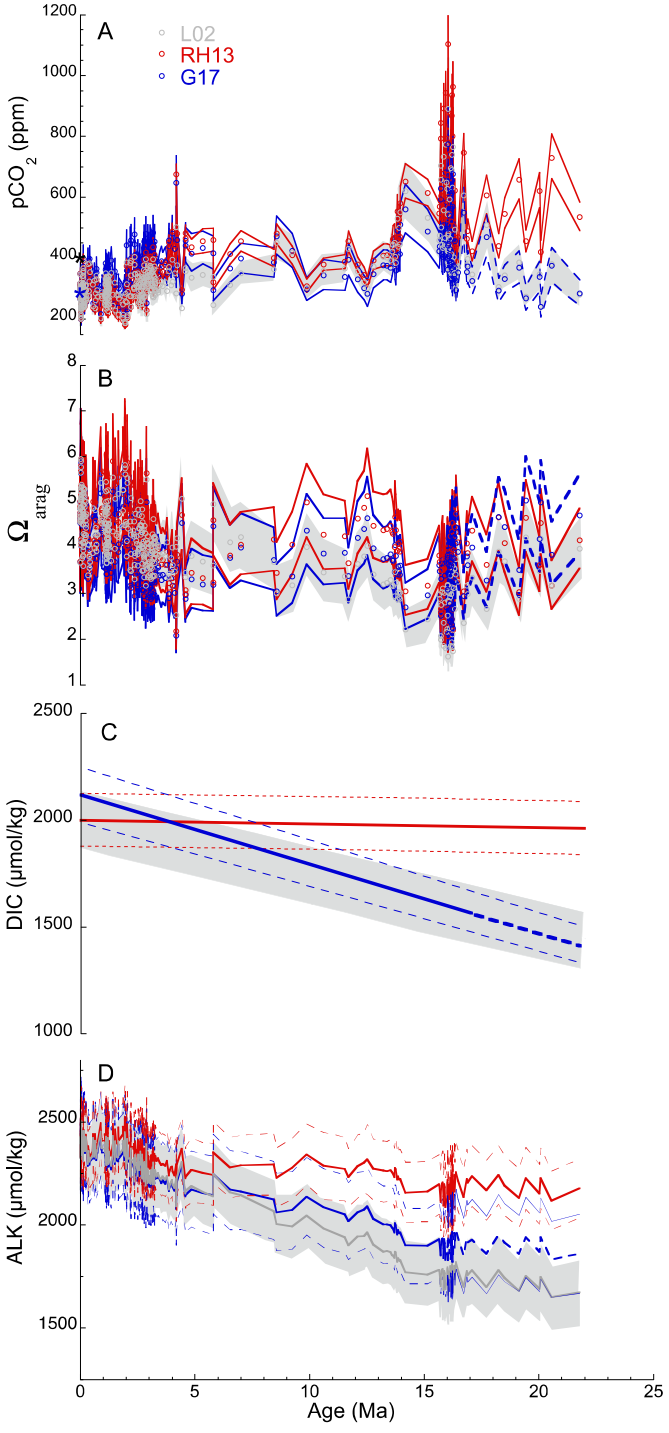

Fig. 4. (A) pCO_2, (B) Ω_{arag}, (C) surface DIC as inferred from deep ocean data (see section 2.4 of text) and (D) ALK reconstructions using three $\delta^{11}B_{sw}$ reconstructions ("$\delta^{11}B_{sw}$-L02"; "$\delta^{11}B_{sw}$-RH13"; "$\delta^{11}B_{sw}$-G17"; Greenop et al., 2017; Raitzsch and Hönisch, 2013, and Lemarchand et al., 2002) and 'Pälike' and 'fluid inclusions' scenarios. 66% confidence intervals are plotted. Dashed lines represent $\delta^{11}B_{sw}$-G17 estimates from >17 Ma to highlight uncertainties associated with the $\delta^{11}B_{sw}$ reconstruction. DIC estimates from the model output of Ridgwell (2005) and Caves et al. (2016) are plotted in panel C. Note CO_2, Ω_{arag} and ALK were calculated based on surface pH reconstruction and long-term DIC trends. (For interpretation of the colours in the figure(s), the reader is referred to the web version of this article.)

their approach, caution should be used when interpreting reconstructions of pH and pCO_2 that are based on their $\delta^{11}B_{sw}$ record (Greenop et al., 2017). Both measurement-based records, RH13 and G17, fall within the uncertainty envelope of L02 modelled reconstruction. However, L02 does not show the same multi-million year variability as RH13 and G17 across the Late Miocene, suggesting that the ocean's input and output of boron that the Lemarchand et al. (2002) model is based on requires further refinement. Overall, we are encouraged by the good agreement between the three independent $\delta^{11}B_{sw}$ records from the Middle Miocene to present, which builds confidence in our reconstructions, but we caution that further refinement is needed in $\delta^{11}B_{sw}$ of the early and late Miocene. Carbonate system data for all $\delta^{11}B_{sw}$ scenarios are provided in the output table (Supplementary Table S6) and discussed further below (see Section 3.3). As the '$\delta^{11}B_{sw} - G17' > 17$ Myr reconstruction is biased by the edge effect we use a dashed line to represent this portion of the pH, CO_2 and Ω_{arag} reconstructions.

As for the history of CCD change, which factors into our estimation of Neogene DIC change, comparing equivalent scenarios with contrasting CCD reconstruction (either Pälike et al., 2012 or Sime et al., 2007) we find only small differences in estimated DIC change (Supplementary Fig. S8), with the scenarios based on the Sime et al. (2007) record consistently resulting in slightly greater rates of long-term DIC increase because of the tendency of long-term CCD deepening in that record (see Supplementary Table S4; Supplementary Fig. S5). This difference between CCD scenarios has only very modest implications for ocean carbon chemistry, consistent with earlier findings (Tyrrell and Zeebe, 2004; Ridgwell, 2005). Consequently, regardless of which CCD reconstruction is used, we arrive at essentially identical reconstructions of CO_2 and Ω_{arag} (Supplementary Fig. S8). This is because the long-term trend in CCD over our study interval (i.e., <500 m) implies only a <8% change in the deep ocean calcium-to-carbonate ion product, DIC, CO_2 and surface saturation state, whereas long-term fractional changes in $[Ca^{2+}]$, benthic $[H^+]$ and surface $[H^+]$ are all much greater. Due to the minor impact the CCD reconstruction has on our results we focus our discussion below on only the scenarios using the CCD reconstruction of Pälike et al. (2012), referred hereafter simply as 'Pälike', because it incorporates data from an array of Pacific DSDP and ODP sediment cores, has better age control, and is of higher resolution.

For our consideration of seawater major ion composition, we carry out our calculations using $[Ca^{2+}]$ and $[Mg^{2+}]$ reconstructions change of Horita et al. (2002) and Brennan et al. (2013) as well as the hypothetical scenario that both concentrations remained unchanged at their modern seawater value throughout the entire study interval (Fig. 3). The reconstructed $[Ca]_{sw}$ derived from fluid inclusions are consistent with calcium isotope model-data comparisons suggesting that $[Ca]_{sw}$ likely decreased through the Neogene (Horita et al., 2002; Heuser et al., 2005; Brennan et al., 2013). Consistent with Hain et al. (2015) we find that the leading order impact of seawater major ion composition operates through $[Ca^{2+}]$ being a direct factor in the $CaCO_3$ solubility product, not through ion–ion interactions and ion-complex formation affecting the equilibrium constants. As described above, using reconstructed deep ocean pH and CCD (the latter as a constraint on the deep ocean calcium-to-carbonate ion product) the reconstructed ~40% secular decline in seawater $[Ca^{2+}]$ over the course of the Neogene translates to a reciprocal secular increase in DIC (Equation (10), Supplementary Fig. S4). Conversely, the general tendency of reconstructed deep ocean pH increase imparts a secular decline in estimated DIC because at higher pH less DIC is needed to maintain a given carbonate ion concentration. That is, in the scenarios that include seawater major ion change the opposing effects of $[Ca^{2+}]$ and benthic pH on estimated DIC partially cancel out, leaving a modest residual long-term DIC rise (Supplementary Fig. S9; Supplementary Table S5; 20 µmol/kg and 27 µmol/kg per million years in the G16 and L02 $\delta^{11}B_{sw}$ scenarios, respectively) or effectively no net DIC change in the case of the RH13 $\delta^{11}B_{sw}$ scenario (3 µmol/kg per million years). Such secular DIC rise during the Neogene is consistent with previous work

(Supplementary Fig. S7; Tyrrell and Zeebe, 2004; Ridgwell, 2005; Caves et al., 2016). As a point of comparison, the hypothetical scenario of time-invariant seawater major ion composition eliminates the calcium-driven tendency of secular increase in DIC, yielding instead long-term estimated DIC decline driven by reconstructed long-term benthic pH rise. With regard to our reconstruction of surface carbon chemistry, which is the product of both our extensive surface pH reconstruction and the long-term trends in DIC that we infer from deep ocean data, the opposing trends in DIC change between the "fluid inclusions" and "constant" scenarios impart opposing tendencies upon reconstructed atmospheric CO_2, with the more realistic "fluid inclusions" scenario exhibiting a reduced secular CO_2 decline (Supplementary Fig. S9). In contrast, our reconstruction of surface carbonate saturation state is virtually insensitive to these scenarios of changing seawater major ion composition (including calcium concentration) (Supplementary Fig. S9). This is largely because our estimate of DIC change is anchored by deep ocean carbonate saturation state via the CCD, which already accounts for seawater major ion composition changes and the strong effect of $[Ca^{2+}]$ change on the carbonate saturation product. In the discussion below we focus exclusively on the "fluid inclusions" scenario because the "constant" scenario is intended only as a sensitivity test and to illustrate our approach to the calculations.

3.3. Neogene pH, CO_2, and Ω_{arag} reconstructions

The calculation of pH and pCO_2 requires records of seawater chemistry (e.g. $\delta^{11}B_{sw}$, $[Ca]_{sw}$) and a second carbonate system parameter (here derived via the CCD) which currently have considerable uncertainties. Based on our sensitivity analysis (Section 3.2), we will discuss three scenarios which uses the L02, and RH13, G17 $\delta^{11}B_{sw}$ reconstructions along with 'Pälike' CCD, and fluid inclusion $[Ca^{2+}]$ and $[Mg^{2+}]$. Late Miocene pH (~8.1) are in agreement with earlier model-based estimates (Ridgwell, 2005). The $\delta^{11}B$-derived CO_2 record from each scenario are in relatively good agreement with published records from a range of proxies (e.g., alkenones, stomata, paleosols) (Zhang et al., 2014; Foster et al., 2017; Supplementary Fig. S10). However, our record shows more structure, with peaks in CO_2 during the MMCO, late Miocene, and late Pliocene (Fig. 4; Supplementary Fig. S10). A particular strength of the $\delta^{11}B$ proxy and our approach is that we also capture simultaneous secular changes in seawater carbonate chemistry.

The most acidic surface conditions (pH~7.6–7.7) occurred in the MMCO where inter-sample variability likely reflects orbital timescale (~100-kyr) cycles associated with large (~200 ppm) CO_2 variations reaching >780–1100 ppm (i.e. max CO_2 value: $891 \pm \frac{165}{135}$ ppm:L02; $1103 \pm \frac{93}{81}$ ppm:RH13; $774 \pm \frac{123}{106}$ ppm:G17) and an average of ~470–630 ppm (i.e. 510 ppm:L02, 630 ppm:RH13, 470 ppm:G17) (Fig. 4; Greenop et al., 2014). Our MMCO surface-water pH estimates are similar to the low values reported for the late Eocene (7.6–7.8; Anagnostou et al., 2016), a time of global warmth, high CO_2 and low ice volume (Lear et al., 2000). Although the rest of the record is at lower resolution and contains sample aliasing of orbital-scale variability, some long-term trends are clearly discernible. Following the MMCO, CO_2 decreased and surface pH increased to ~8.1 at 12.5 Ma, similar to pre-industrial (Figs. 2, 4). Surface pH was ~8.0–8.1 between 9 and 3 Myr and subsequently increased towards the late Pleistocene glacial/interglacial range of ~8.3 to ~8.1 (Foster, 2008; Hönisch et al., 2009; Henehan et al., 2013; Chalk et al., 2017).

Unlike the oscillations in pH and CO_2, our record of low latitude aragonite saturation (Ω_{arag}) is broadly constant being in the range 3 to 5 for much of the last 24 million years. In detail however mean low latitude Ω_{arag} increased from the MMCO

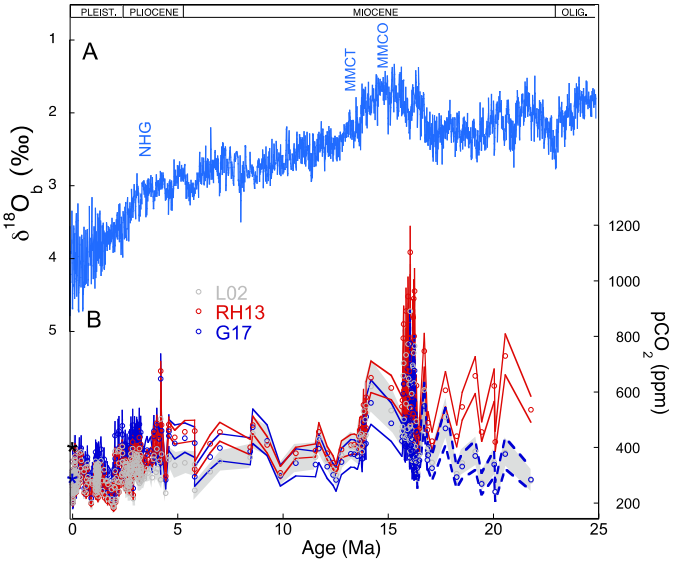

Fig. 5. (A) $\delta^{18}O_b$ stack (Zachos et al., 2008) and (B) CO_2 records from this study using $\delta^{11}B_{sw}$-L02, $\delta^{11}B_{sw}$-RH13, and $\delta^{11}B_{sw}$-G17 reconstructions with 'Pälike' and 'fluid inclusions scenarios; 66% confidence intervals are plotted.

(2.7 ± 0.5:L02; 3.5 ± 0.6:RH13; 3.3 ± 0.6:G17) to relatively stable levels (3.8 ± 0.7:L02; 4.0 ± 0.7:RH13; 3.7 ± 0.7:G17) in the late Miocene with near pre-industrial values (4.1 ± 0.8:L02; 4.3 ± 0.8:RH13; 3.7 ± 0.7:G17) first being reached in the late Pliocene-early Pleistocene (Fig. 4). As with the apparent orbital scale fluctuations in reconstructed MMCO pCO_2, the pH fluctuations implied by the Greenop et al. (2014) boron isotope data result in substantial fluctuations in reconstructed saturation state, with the MMCO episodes of low pH corresponding to the lowest saturation levels (1.6–2.1) that we find over the entire Neogene study interval.

It is worth noting that the rather large uncertainty intervals we report for each of a number of scenarios are the result of conservative propagation of uncertainty in the various input parameters. Only a small proportion of that uncertainty is due to the $\delta^{11}B$ measurements and the other proxy data required for the boron isotope pH proxy. Instead, structural uncertainty in seawater composition – major ion, $\delta^{11}B_{sw}$, DIC – are compounded in our approach to reconstruct seawater carbonate chemistry over geologic time-scales much longer than the residence time of each of these constituents. To illustrate that point we consider an alternative scenario for the Plio-Pleistocene (Supplementary Fig. S11), a geologically recent interval where seawater major ion, $\delta^{11}B_{sw}$, DIC can be anchored at modern values and their structural uncertainty is usefully assessed through the spread in the respective scenarios. For this alternative scenario we propagate the uncertainties due to the spread of $\delta^{11}B_{sw}$ reconstructions and the spread in our scenarios of long-term DIC drift under the 'fluid inclusion' major ion scenario, while maintaining the propagation of uncertainties in temperature, salinity and foraminiferal $\delta^{11}B$ the same. In that scenario we find uncertainty intervals for pH, CO_2 and carbonate saturation states small enough to confidently resolve glacial/interglacial cycles, something not possible with our treatment of the full Neogene dataset (Supplementary Fig. S11; Supplementary Table S7). That is, while our approach to reconstruct seawater carbonate chemistry of the Neogene is able to resolve long-term trends and large magnitude episodes such as the MMCO there remains considerable room for improving the reconstructions by reducing uncertainties related to seawater composition.

3.4. Evaluating Miocene CO_2-climate decoupling

Long-term climate trends across the Neogene, as inferred from benthic foraminiferal $\delta^{18}O_b$ records, show a transition from an extended period of global warmth of the MMCO to the modern icehouse world marked by the Middle Miocene Climate Transition (MMCT) at 13.9 Ma where Antarctic ice sheets expanded and climate cooled (Fig. 5; Zachos et al., 2001, 2008; Cramer et al., 2009; Lear et al., 2010). Following this global cooling step, the lack of trend in the $\delta^{18}O_b$ record suggests that Earth's climate was relatively stable during the late Miocene (11.6–5.3 Ma) (Zachos et al., 2001, 2008). However, a recent global SST compilation indicates a long-term surface cooling across this interval reaching near modern ocean temperatures between 5 and 7.4 Myrs ago (Herbert et al., 2016). In contrast to the late Miocene, the early Pliocene was a period of prolonged warmth terminated at 2.7 Ma with the initiation of northern hemisphere glaciation and subsequent intensification of glacial interglacial climate variability in the Pleistocene (Lisiecki and Raymo, 2005). Previous CO_2 records suggest that the transition from the warm MMCO to the cooler post-MMCT was associated with a decline in CO_2 (Kürschner et al., 2008; Foster et al., 2012). The warmth of the early Pliocene has also been previously attributed to higher than pre-industrial atmospheric CO_2 levels (Seki et al., 2010; Bartoli et al., 2011; Martínez-Botí et al., 2015a). However, the role of CO_2 in evolution of global climate across the Late Miocene is still under debate.

Alkenone-derived CO_2 records from Pagani et al. (1999a, 1999b) exhibited low CO_2 levels during the early to mid Miocene with no significant shifts in the late Miocene. This led the authors to identify no long-term correlation of climate and CO_2 and suggest a late Miocene decoupling between CO_2 and climate (Pagani et al., 1999a, 1999b, 2005). However, subsequent work has shown that foraminifera-$\delta^{18}O$ based SST estimates used in these late Miocene alkenone-CO_2 calculations were too low due to inaccuracies in their estimates of ice volume, calcification depth, and diagenetic overprint (Pagani et al., 2010). Subsequent TEX_{86} derived SST estimates indicate relatively higher temperatures that would suggest higher CO_2 levels than previously published, but still supporting a decoupling between climate and CO_2 in the late Miocene (Zhang et al., 2014).

Late Miocene climate records suggesting warmer than modern continental and oceanic temperatures and the relatively low alkenone-based CO_2 levels are therefore difficult to reconcile with a dominant role of CO_2 in setting the evolution of late Miocene climate (Pound et al., 2011; LaRiviere et al., 2012). Specifically, LaRiviere et al. (2012) shows that North Pacific SSTs were significantly higher than today and suggest that in the absence of significantly elevated CO_2, a complex mechanism involving a deepened thermocline, expansion of tropical warm pool and increased water vapour may have maintained the late Miocene warmth. Here we use our new Neogene CO_2 records to examine the degree of coherency between CO_2 and $\delta^{18}O_b$ and revisit the idea of climate-CO_2 decoupling in the Miocene.

Cross-plots between CO_2 climate forcing (i.e., a linear function of the logarithm of CO_2, i.e., $\ln(CO_2/278)$; Myhre et al., 1998) and $\delta^{18}O_b$, for all three $\delta^{11}B_{sw}$ scenarios, show a correlation across the Mid-Miocene (11.6–16 Ma) and Pliocene (0–5 Ma) (Fig. 6). The good correspondence between CO_2 and $\delta^{18}O_b$ across these time intervals suggests a dominant role for CO_2 in forcing climate. Despite this good coupling between global climate (as recorded by benthic $\delta^{18}O$) and CO_2 for the Plio-Pleistocene and Mid Miocene, across the late Miocene (5.3–11.6 Ma) we record CO_2 changes that are not strongly matched by corresponding changes in the $\delta^{18}O_b$ record (i.e. no variance in $\delta^{18}O_b$ that corresponds to the variance in our reconstructed CO_2; $R^2 = 0.02$–0.09; Figs. 5; 6). Regardless of the chosen $\delta^{11}B_{sw}$ scenario, all our CO_2 reconstructions shows CO_2

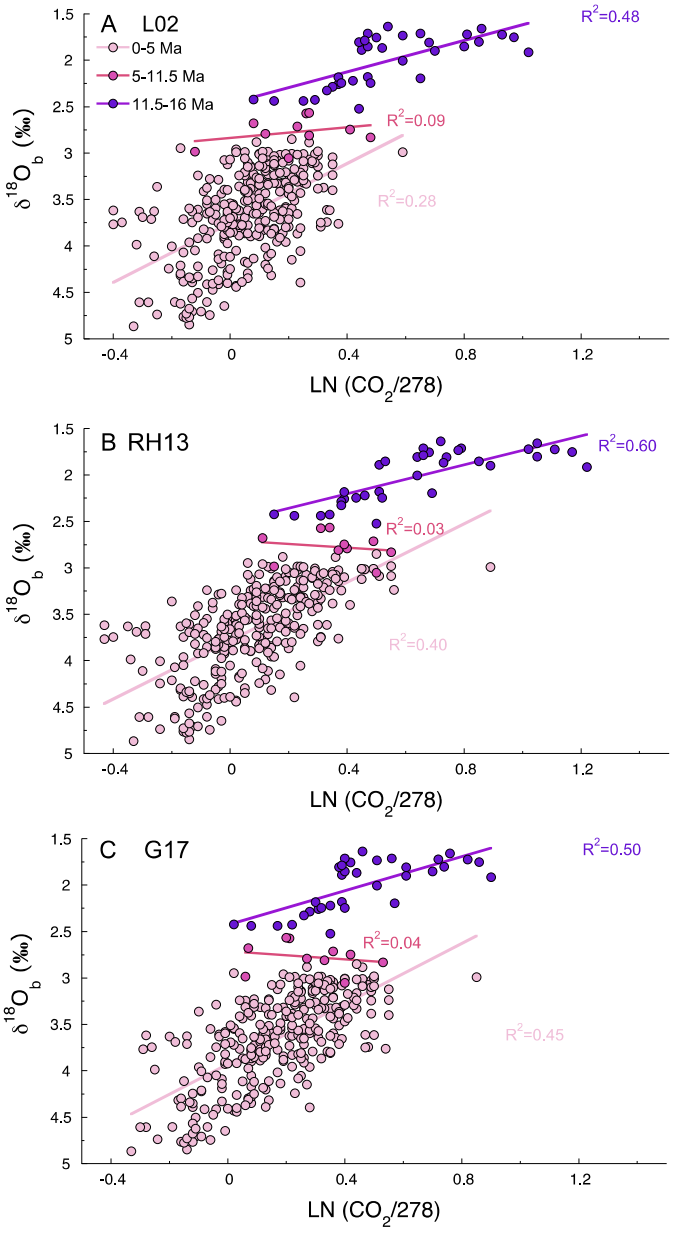

Fig. 6. Mid-Miocene (11.6–16 Ma), late Miocene (5.3–11.6 Ma), and Plio-Pleistocene (5.3–0 Ma) CO_2 forcing, expressed as LN (CO_2/278) in comparison to interpolated $\delta^{18}O_b$ (Zachos et al., 2008). CO_2 reconstruction used in this comparison is from all $\delta^{11}B_{sw}$ scenarios (G17, RH13, L02) and 'Pälike' and 'fluid inclusions' reconstructions.

peak at ~9 Ma that is not seen in the climate records (Fig. 5). This peak in CO_2 at ~9 Ma is also seen in recent cell-sized corrected alkenones and pennate diatoms (diffusive and ACTI-CO models) CO_2 records (Bolton et al., 2016; Mejía et al., 2017; Supplementary Fig. S12). However, quantification of the CO_2 variations using the diatom method awaits determination of a diatom active carbon uptake model. Nonetheless, the convergence in CO_2 trends from 11.6 to 8.5 Ma and the mismatch between CO_2 and climate trends support the notion of a late Miocene "climate-CO_2 decoupling" (Pagani et al., 1999a, 1999b). This could reflect the significance of oceanographic or palaeogeographic changes and related feedbacks in setting the late Miocene climate, as suggested by others (Pagani et al., 1999a, 1999b; Foster et al., 2010; LaRiviere et al., 2012), which may have masked or counteracted changes in the CO_2 forcing at this time.

However, there remain two principle caveats that prevent definite verification of the apparent late Miocene decoupling of CO_2

and climate with our current CO_2 record: (1) while we present the highest resolution late Miocene CO_2 reconstruction to date, our record still does not resolve CO_2 change at an orbital timescale and may thus contain aliasing of orbital scale CO_2 variability, and (2) during the late Miocene there is growing evidence for rapid and large magnitude $\delta^{11}B_{sw}$ change, evident in the two measurement-based $\delta^{11}B_{sw}$ records (RH13 and G17) (Fig. 2). Boron isotope based reconstructions of carbon cycle and CO_2 change during this period critically depends on reconstructions that correctly capture both the pace and timing of this $\delta^{11}B_{sw}$ shift. Interestingly, there is a correlation of our planktic $\delta^{11}B$ to $\delta^{18}O_b$ ($R^2 = 0.22$) that is not evident in CO_2 calculated from the boron isotope data (Supplementary Fig. S13). This observation could be used to argue that some intervals of late Miocene carbon cycle change may in fact have changed in tune with climate but this relationship is currently obscured by the uncertainties in the parameters needed to convert $\delta^{11}B$ to CO_2 (and pH). Therefore, a detailed and robust record of $\delta^{11}B_{sw}$ change across the late Miocene is needed to fully elucidate the nature of CO_2-climate coupling at this time.

3.5. Geological context of future ocean acidification

Over the last 250 yrs, anthropogenic emissions have increased atmospheric CO_2 levels by >40% to ~400 ppm (Keeling et al., 2001; Betts et al., 2016; https://www.co2.earth) more than 120 ppm above the range of glacial–interglacial cycles of at least the last 800,000 yrs (Petit et al., 1999; Siegenthaler et al., 2005; Luethi et al., 2008; Bereiter et al., 2015). The oceans have absorbed about a third of the CO_2 emitted since the 1750s (Doney et al., 2009; Le Quere et al., 2016), with the CO_2 titrating ocean carbonate ion so as to simultaneously decrease pH and calcium carbonate saturation state. Predictions of future pH and saturation state are widely regarded as sufficient to disrupt physiological processes and reduce calcification, development, and fecundity in a range of marine organisms (Gattuso et al., 2015). Furthermore, reduced pH will impact the availability of essential nutrients (i.e. N) and trace metals (i.e. Fe) critical to marine primary producers for biological functions, altering marine biogeochemical cycles (Hutchins et al., 2007; Hoffmann et al., 2012).

In Fig. 7 we compare our geological record of pH and CO_2 to future predictions based on IPCC Representative Concentration Pathway (RCP) scenarios from the stringent (RCP2.6) to the high-carbon business as usual trajectory (BAU; RCP8.5) which extend to 2100 (Bopp et al., 2013). Note we limit our discussion here to MC-ICPMS based pH, CO_2, and Ω_{arag} dataset (Seki et al., 2010; Foster et al., 2012; Badger et al., 2013; Greenop et al., 2014; Martínez-Botí et al., 2015a; Chalk et al., 2017; this study), to maintain internal consistency free of poorly defined analytical offsets (see previous discussion). Because ocean acidification will continue beyond 2100, we also make the comparison with estimates up to the year 2500 using emission pathways releasing 250 PgC and 2000 PgC (the near equivalent to RCP2.6 and BAU RCP8.5, respectively), 5000 PgC (a possible upper limit including unconventional fossil fuels such as shale gas), and 10,000 PgC (a possible upper limit on all available carbon resources) (Winkelmann et al., 2015; Bruckner et al., 2014). To compare our low latitude specific Ω_{arag} to the global average as presented in Winkelmann et al. (2015) model, we adjust model Ω_{arag} by a constant offset (i.e. 0.9) based on the pre-industrial difference between low latitude and global model estimates. Current CO_2 reconstructions of 400 ppm (Keeling et al., 2001; Betts et al., 2016; https://www.co2.earth) are similar to the highest values we reconstruct during the interglacials of the Pliocene and in late Miocene. By 2100, pH levels on the RCP8.5 pathway will be <7.8 and CO_2 near 930 ppm, unprecedented for the last 14 million years (66% CI). If continued unabated (following the 2000 PgC emission pathway) conditions will reach a pH as low as 7.7 by 2150 and CO_2 as high 960 ppm, equivalent to some of the lowest MMCO levels (66% CI). Exhaustion of conventional and unconventional (10,000 PgC) fossil fuel reserves could reduce pH to 7.2 and increase CO_2 to ~4200 ppm by 2300 (Bruckner et al., 2014; Winkelmann et al., 2015), unprecedented in at least 22 Myr (at 66% confidence). By 2100 Ω_{arag} levels will be <2.75 in the BAU scenarios, lower than any point in the last 8 million years (66% CI) in two scenarios. Further CO_2 emissions predict Ω_{arag} to reach globally undersaturated conditions. The only parallels of such extreme and geologically rapid acidification in the geological past is associated with major mass extinction (Clarkson et al., 2015).

On geologic timescales (>10,000 yrs), the balance between the delivery and removal of alkalinity to the oceans via carbonate weathering and burial acts to partially decouple pH and carbonate saturation state (Fig. 4; Hönisch et al., 2012). Previous studies suggest that surface ocean saturation state was relatively constant across the last 65 Myrs excluding short-term events such as Eocene–Oligocene Transition and Paleocene–Eocene Thermal Maximum (Tyrrell and Zeebe, 2004; Ridgwell and Zeebe, 2005; Hönisch et al., 2012; Pälike et al., 2012; Zeebe, 2012; Penman et al., 2014). However, these Cenozoic records of Ω rely on carbon cycle models that make significant assumptions about CO_2 across the time interval. Our record of the ocean carbonate system shows broadly constant values for the Neogene in the range 3–5, but with clear minimum Ω_{arag} values, lower than pre-industrial levels, during the warmth of the MMCO when pH values are the lowest in our record (Figs. 2, 4). Pacific % carbonate records (Holbourn et al., 2013) indicate that there were large changes in the CCD on glacial–interglacial timescales during the MMCO indicating a dynamic carbon cycle. The fossil record shows significant global and regional extinction of corals and molluscs in the early and middle Miocene, although arguably not an extraordinary occurrence, while calcifying plankton thrived during the MMCO (Budd, 2000; Warren and Bottier, 2001; Bown et al., 2004; Ezard et al., 2011). Considering the possible consequences of ongoing acidification for marine organisms, however, one must balance these observations with the fact that geological rates of change were much slower leading into the MMCO than current anthropogenic change, allowing for more time for species to adapt (e.g. scleractinian reefs in the middle Miocene; Perrin, 2002; Wilson, 2008; Hönisch et al., 2012).

The existence of past warm climates, combined with a history of glacial–interglacial variability suggests that, if given time, many calcifiers may be able to adapt to slightly more acidic and less saturated waters than occur at present. However there is no clear analogue for the rate and magnitude of change over the coming centuries under BAU emissions scenarios. End-of-century BAU pH predictions are comparable to the long-term pH regime (pH < 7.8) experienced in natural CO_2 seep sites, suggesting future, acclimatized tropical ecosystems may have a lower species diversity with higher number of acidification tolerant species (Hofmann et al., 2011; Fabricius et al., 2011). Reduced pH will alter the biogeochemical cycling and the ocean inventory on nutrients and trace metals, which can significantly impact marine biota function under future CO_2 scenarios (Hutchins et al., 2007; Hoffman et al., 2012). Moreover, ocean acidification coincides with warming and other environmental stresses, potentially exacerbating these negative effects (Gattuso et al., 2015). The current pH of the surface ocean is already probably lower than at any time in the last 2 Myr and the rate of acidification is increasing (Hönisch et al., 2009; IPCC, 2014). Some organisms are already negatively impacted (Bednarsek et al., 2012). The predicted changes in pH and saturation state constitute a substantial threat to marine life, especially for the higher emissions scenarios in which the chemistry of the open ocean is forced, with unprecedented rapidity, into a state that is clearly well be-

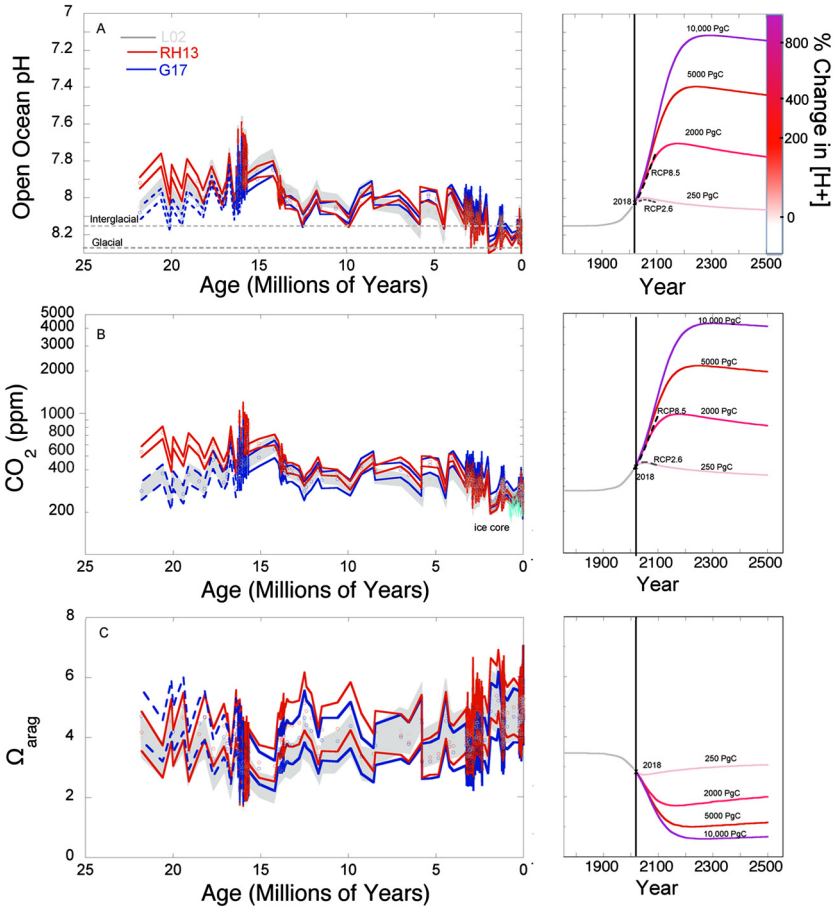

Fig. 7. (A) Open ocean pH reconstruction with 66% CI error envelope. Dashed lines represent average late Pleistocene interglacial and glacial pH values (Foster, 2008; Hönisch et al., 2009). Highlighted on the right *y*-axis is percent difference in $[H^+]$ from preindustrial levels. B) CO_2, plotted on the log scale reconstruction with Monte Carlo uncertainty estimates (66% CI). Ice core CO_2 data for the last 0.8 Myr are plotted in blue (Petit et al., 1999; Siegenthaler et al., 2005; Luethi et al., 2008; Bereiter et al., 2015). (C) Low latitude surface ocean aragonite saturation (Ω_{arag}) reconstruction with Monte Carlo uncertainty estimates (66% CI). pH, pCO_2, and Ω_{arag} reconstructions derived from scenarios using $\delta^{11}B_{sw}$-L02 (grey), $\delta^{11}B_{sw}$-RH13 (red), $\delta^{11}B_{sw}$-G17 (blue) and 'Pälike' and 'fluid inclusions'. pH and pCO_2 predictions derive from RCP2.6 and RCP 8.5 IPCC pathways (Bopp et al., 2013) and GENIE model output from Winklemann et al. (2015) with century-scale pathways from 2010–2500 with range of post-2010 CO_2 additions (250, 2000, 5000, and 10,000 PgC). Ω_{arag} predictions derives from GENIE model output only. Note RCP2.6 and RCP8.5 IPCC pathways follow post-2012 CO_2 emissions of $270\pm^{170}_{130}$ and $1685\pm^{225}_{270}$ PgC.

yond the long-term natural baseline of the last millions to tens of millions of years as established in this study (Fig. 7).

4. Conclusions

Here we present a Neogene record of planktic foraminiferal $\delta^{11}B$ from which we estimate surface water pH and Ω_{arag} as well as atmospheric CO_2. These calculations also incorporate previous reconstructions of seawater $\delta^{11}B$ ($\delta^{11}B_{sw}$), major ion composition and deep sea carbonate burial (i.e., CCD). Our sensitivity analysis demonstrates that different $\delta^{11}B_{sw}$ reconstructions influence our estimates of both pH and CO_2, most significantly during the early and late Miocene when $\delta^{11}B_{sw}$ reconstructions diverge. Additionally, the reconstructed secular decline in seawater calcium concentration implies a secular DIC increase that counteracts a portion of reconstructed pH-rise-driven secular CO_2 decline but has only a weak effect on reconstructed surface aragonite saturation state. The choice of CCD record used in the reconstruction of DIC has mostly insignificant effects on our reconstructions. Our pH records suggests that the lowest pH of the past 22 Myr occurred in the Middle Miocene Climatic Optimum, when pH levels were similar to those of the early Cenozoic. This interval of global warmth is associated with average CO_2 in all our scenarios, reaching >470–630 ppm. Following the MMCO there is a general long-term trend towards lower CO_2 as climate cooled towards the Pleistocene. Superimposed on this trend is an apparent CO_2 peak at ~9 Ma, reproduced in all scenarios, that is not matched by corresponding changes in SST and $\delta^{18}O_b$ records. However, to definitely resolve the degree climate–carbon cycle coupling of the late Miocene will require more detailed records of the pace and magnitude of $\delta^{11}B_{sw}$ change during that interval. Finally, we show that it is unlikely that marine ecosystems experienced low latitude surface pH and Ω_{arag} below 7.7 and 1.7 respectively during the past 14 million years (66% CI). Under business as usual scenarios MMCO CO_2 and pH levels will be reached by 2100 and Ω_{arag} will be lower than any point in the last 14 million years (66% CI). Understanding the full implication of this conclusion requires long-term laboratory and field studies examining physiological and ecosystem responses to the full range of biogeochemical changes associated with ocean acidification as well as additional observations from the fossil record.

Acknowledgements

This study used samples provided by the International Ocean Discovery Program (IODP). We thank A. Milton at the University of Southampton for maintaining the mass spectrometers used in this study. We thank D. Schmidt for help with sample selection from ODP site 1000A. This work was funded by NERC Grant NE/I006427/1 (CHL and GLF). PNP and GLF were supported by

NERC/DEFRA/DECC Grant NE/H017581/1 (U.K. Ocean Acidification Research Programme). MPH was supported by NERC fellowship (NE/K00901X/1). SMS acknowledges the financial support provided by the Welsh Government and Higher Education Funding Council for Wales through the Sêr Cymru National Research Network for Low Carbon, Energy and Environment Returning Fellowship.

Appendix A. Supplementary material

Supplementary material related to this article can be found online at https://doi.org/10.1016/j.epsl.2018.06.017.

References

Anagnostou, E., John, E.H., Edgar, K.M., Foster, G.L., Ridgwell, A., Inglis, G.N., Pancost, R.D., Lunt, D.J., Pearson, P.N., 2016. Changing atmospheric CO_2 concentration was the primary driver of early Cenozoic climate. Nature 533, 380–384.

Anand, P., Elderfield, H., Conte, M.H., 2003. Calibration of Mg/Ca thermometry in planktonic foraminifera from a sediment trap time series. Paleoceanography 18.

Andre, A., Weiner, A., Quillevere, F., Aurahs, R., Morard, R., Douady, C.J., de Garidel-Thoron, T., Escarguel, G., de Vargas, C., Kucera, M., 2013. The cryptic and the apparent reversed: lack of genetic differentiation within the morphologically diverse plexus of the planktonic foraminifer Globigerinoides sacculifer. Paleobiology 39, 21–39.

Badger, M.P.S., Lear, C.H., Pancost, R.D., Foster, G.L., Bailey, T.R., Leng, M.J., Abels, H.A., 2013. CO_2 drawdown following the middle Miocene expansion of the Antarctic Ice Sheet. Paleoceanography 28.

Barker, S., Greaves, M., Elderfield, H., 2003. A study of cleaning procedures used for foraminiferal Mg/Ca paleothermometry. Geochem. Geophys. Geosyst. 4.

Bartoli, G., Hönisch, B., Zeebe, R.E., 2011. Atmospheric CO_2 decline during the Pliocene intensification of Northern Hemisphere glaciations. Paleoceanography 26.

Bednarsek, N., Tarling, G.A., Bakker, D.C.E., Fielding, S., Jones, E.M., Venables, H.J., Ward, P., Kuzirian, A., Leze, B., Feely, R.A., Murphy, E.J., 2012. Extensive dissolution of live pteropods in the Southern Ocean. Nat. Geosci. 5, 881–885.

Bereiter, B., Eggleston, S., Schmitt, J., Nehrbass-Ahles, C., Stocker, T.F., Fischer, H., Kipfstuhl, S., Chappellaz, J., 2015. Revision of the EPICA Dome C CO_2 record from 800 to 600 kyr before present. Geophys. Res. Lett. 42, 542–549.

Betts, R.A., Jones, C.D., Knight, J.R., Keeling, R.F., Kennedy, J.J., 2016. El Nino and a record CO_2 rise. Nat. Climate Change 6, 806–810.

Birch, H., Coxall, H.K., Pearson, P.N., Kroon, D., O'Regan, M., 2013. Planktonic foraminifera stable isotopes and water column structure: disentangling ecological signals. Mar. Micropaleontol. 101, 127–145.

Bolton, C.T., Hernandez-Sanchez, M.T., Fuertes, M.A., Gonzalez-Lemos, S., Abrevaya, L., Mendez-Vicente, A., Flores, J.A., Probert, I., Giosan, L., Johnson, J., Stoll, H.M., 2016. Decrease in coccolithophore calcification and CO_2 since the middle Miocene. Nat. Commun. 7, 13.

Bopp, L., Resplandy, L., Orr, J.C., Doney, S.C., Dunne, J.P., Gehlen, M., Halloran, P., Heinze, C., Ilyina, T., Seferian, R., Tjiputra, J., Vichi, M., 2013. Multiple stressors of ocean ecosystems in the 21st century: projections with CMIP5 models. Biogeosciences 10, 6225–6245.

Bown, P.R., Lees, J.A., Young, J.R., 2004. Calcareous nannoplankton evolution and diversity through time. In: Coccolithophores: from Molecular Processes to Global Impact, pp. 481–508.

Brennan, S.T., Lowenstein, T.K., Cendon, D.I., 2013. The major ion composition of Cenozoic seawater: the past 36 million years from fluid inclusions in marine halite. Am. J. Sci. 313, 713–775.

Bruckner, J., et al., 2014. Energy systems. In: Climate Change 2014: Mitigation of Climate Change. Contribution of Working Group III to the Fifth Assessment Report of the Intergovernmental Panel on Climate Change. Cambridge University Press, Cambridge, United Kingdom and New York, NY, USA.

Budd, A.F., 2000. Diversity and extinction in the Cenozoic history of Caribbean reefs. Coral Reefs 19, 25–35. https://doi.org/10.1007/s003380050222.

Cande, S.C., Kent, D.V., 1995. Revised calibration of the geomagnetic polarity timescale for the late Cretaceous and Cenozoic. J. Geophys. Res., Solid Earth 100, 6093–6095.

Catanzaro, E.J., et al., 1970. Boric Acid; Isotopic, and Assay Standard Reference Materials. US National Bureau of Standards Special Publication 260-17.

Caves, J.K., Jost, A.B., Lau, K.V., Maher, K., 2016. Cenozoic carbon cycle imbalances and a variable silicate weathering feedback. Earth Planet. Sci. Lett. 450, 152–163. https://doi.org/10.1016/j.epsl.2016.06.035.

Chaisson, W.P., Pearson, P.N., 1997. Planktonic foraminifer biostratigraphy at Site 925: middle Miocene–Pleistocene. In: Shackleton, N.J., Curry, W.B., Richter, C., Bralower, T.J. (Eds.), Proc. ODP, Sci. Results, 154: College Station, TX (Ocean Drilling Program), pp. 3–31.

Chalk, T.B., Hain, M.P., Foster, G.L., Rohling, E.J., Sexton, P.F., Badger, M.P.S., Cherry, S.G., Hasenfratz, A.P., Haug, G.H., Jaccard, S.L., Martínez-García, A., Pälike, H., Pancost, R.D., Wilson, P.A., 2017. Causes of ice age intensification across the Mid-Pleistocene transition. Proc. Natl. Acad. Sci. USA. https://doi.org/10.1073/pnas.1702143114.

Clarkson, M.O., Kasemann, S.A., Wood, R.A., Lenton, T.M., Daines, S.J., Richoz, S., Ohnemueller, F., Meixner, A., Poulton, S.W., Tipper, E.T., 2015. Ocean acidification and the Permo–Triassic mass extinction. Science 348, 229–232.

Cramer, B.S., Toggweiler, J.R., Wright, J.D., Katz, M.E., Miller, K.G., 2009. Ocean overturning since the Late Cretaceous: inferences from a new benthic foraminiferal isotope compilation. Paleoceanography 24.

Delaney, M.L., Be, A.W.H., Boyle, E.A., 1985. Li, Sr, Mg, and Na in foraminiferal calcite shells from laboratory culture, sediment traps, and sediment cores. Geochim. Cosmochim. Acta 49, 1327–1341.

Derry, L.A., France-Lanord, C., 1996. Neogene growth of the sedimentary organic carbon reservoir. Paleoceanography 11, 267–275.

Dickson, A.G., 1990. Thermodynamics of the dissociation of boric-acid in synthetic seawater from 273.15-K to 318.15-K. Deep-Sea Res., A, Oceanogr. Res. Pap. 37, 755–766.

Doney, S.C., Fabry, V.J., Feely, R.A., Kleypas, J.A., 2009. Ocean acidification: the other CO_2 problem. Annu. Rev. Mar. Sci. 1, 169–192.

Edgar, K.M., Anagnostou, E., Pearson, P.N., Foster, G.L., 2015. Assessing the impact of diagenesis on delta B-11, delta C-13, delta O-18, Sr/Ca and B/Ca values in fossil planktic foraminiferal calcite. Geochim. Cosmochim. Acta 166, 189–209.

Evans, D., Mueller, W., 2012. Deep time foraminifera Mg/Ca paleothermometry: nonlinear correction for secular change in seawater Mg/Ca. Paleoceanography 27.

Ezard, T.H.G., Aze, T., Pearson, P.N., Purvis, A., 2011. Interplay between changing climate and species' ecology drives macroevolutionary dynamics. Science 332, 349–351. https://doi.org/10.1126/science.1203060.

Fabricius, K.E., Langdon, C., Uthicke, S., Humphrey, C., Noonan, S., De'ath, G., Okazaki, R., Muehllehner, N., Glas, M.S., Lough, J.M., 2011. Losers and winners in coral reefs acclimatized to elevated carbon dioxide concentrations. Nat. Climate Change 1, 165–169.

Farmer, J.R., Hönisch, B., Uchikawa, J., 2016. Single laboratory comparison of MC-ICP-MS and N-TIMS boron isotope analyses in marine carbonates. Chem. Geol. 447, 173–182.

Foster, G.L., 2008. Seawater pH, pCO_2 and $[CO_3^{-2}]$ variations in the Caribbean Sea over the last 130 kyr: a boron isotope and B/Ca study of planktic foraminifera. Earth Planet. Sci. Lett. 271 (1–4), 254–266. https://doi.org/10.1016/j.epsl.2008.04.015.

Foster, G.L., Lunt, D.J., Parrish, R.R., 2010. Mountain uplift and glaciation of North America – a sensitivity study. Clim. Past 6, 707–717. https://doi.org/10.5194/cp-6-707-2010.

Foster, G.L., Lear, C.H., Rae, J.W.B., 2012. The evolution of pCO_2, ice volume and climate during the middle Miocene. Earth Planet. Sci. Lett. 341, 243–254.

Foster, G.L., Hönisch, B., Paris, G., Dwyer, G.S., Rae, J.W.B., Elliott, T., Gaillardet, J., Hemming, N.G., Louvat, P., Vengosh, A., 2013. Interlaboratory comparison of boron isotope analyses of boric acid, seawater and marine $CaCO_3$ by MC-ICPMS and NTIMS. Chem. Geol. 358, 1–14.

Foster, G.L., Rae, J.W.B., 2016. Reconstructing ocean pH with boron isotopes in foraminifera. In: Jeanloz, R., Freeman, K.H. (Eds.), Annual Review of Earth and Planetary Sciences, vol. 44, pp. 207–237.

Foster, G.L., Royer, D., Lunt, D.J., 2017. Future climate forcing potentially without precedent in the last 420 million years. Nat. Commun. 8, 14845. https://doi.org/10.1038/ncomms14845.

France-Lanord, C., Derry, L.A., 1997. Organic carbon burial forcing of the carbon cycle from Himalayan erosion. Nature 390, 65–67.

Gattuso, J.P., Magnan, A., Bille, R., Cheung, W.W.L., Howes, E.L., Joos, F., Allemand, D., Bopp, L., Cooley, S.R., Eakin, C.M., Hoegh-Guldberg, O., Kelly, R.P., Poertner, H.O., Rogers, A.D., Baxter, J.M., Laffoley, D., Osborn, D., Rankovic, A., Rochette, J., Sumaila, U.R., Treyer, S., Turley, C., 2015. Contrasting futures for ocean and society from different anthropogenic CO_2 emissions scenarios. Science 349, 45.

Greenop, R., Foster, G.L., Wilson, P.A., Lear, C.H., 2014. Middle Miocene climate instability associated with high-amplitude CO_2 variability. Paleoceanography 29, 845–853.

Greenop, R., Foster, G.L., Sosdian, S.M., Hain, M.P., Oliver, K.I.C., Chalk, T.B., Lear, C.H., Wilson, P.A., 2017. A record of Neogene seawater $\delta^{11}B$ calculated from paired $\delta^{11}B$ analyses on benthic and planktonic foraminiferal. Clim. Past 13, 149–170. https://doi.org/10.5194/cp-13-149-2017.

Gutjahr, M., Ridgwell, A., Sexton, P.F., Anagnostou, E., Pearson, P.N., Pälike, H., Norris, R.D., Thomas, E., Foster, G.L., 2017. Very large release of mostly volcanic carbon during the Palaeocene–Eocene Thermal Maximum. Nature 548, 573.

Hain, M.P., Sigman, D.M., Higgins, J.A., Haug, G.H., 2015. The effects of secular calcium and magnesium concentration changes on the thermodynamics of seawater acid/base chemistry: implications for Eocene and Cretaceous ocean carbon chemistry and buffering. Glob. Biogeochem. Cycles 29, 517–533.

Harvie, C.E., Moller, N., Weare, J.H., 1984. The prediction of mineral solubilities in natural-waters—the $Na–K–Mg–Ca–H–Cl–SO_4–OH–HCO_3–CO_3–CO_2–H_2O$ system to high ionic strengths at 25°C. Geochim. Cosmochim. Acta 48 (4), 723–751.

Hasiuk, F.J., Lohmann, K.C., 2010. Application of calcite Mg partitioning functions to the reconstruction of paleocean Mg/Ca. Geochim. Cosmochim. Acta 74, 6751–6763.

Hathorne, E.C., Gagnon, A., Felis, T., Adkins, J., Asami, R., Boer, W., Caillon, N., Case, D., Cobb, K.M., Douville, E., deMenocal, P., Eisenhauer, A., Garbe-Schonberg, D., Geibert, W., Goldstein, S., Hughen, K., Inoue, M., Kawahata, H., Kolling, M., Cornec, F.L., Linsley, B.K., McGregor, H.V., Montagna, P., Nurhati, I.S., Quinn, T.M., Raddatz, J., Rebaubier, H., Robinson, L.F., Sadekov, A., Sherrell, R., Sinclair, D., Tudhope, A.W., Wei, G.J., Wong, H.R., Wu, H.C., You, C.F., 2013. Interlaboratory study for coral Sr/Ca and other element/Ca ratio measurements. Geochem. Geophys. Geosyst. 14, 3730–3750.

He, S.L., Morse, J.W., 1993. The carbonic-acid system and calcite solubility in aqueous Na–K–Ca–MgCl–SO_4 solutions from 0 to 90 °C. Geochim. Cosmochim. Acta 57 (15), 3533–3554.

Hemming, N.G., Hanson, G.N., 1992. Boron isotopic composition and concentration in modern marin carbonates. Geochim. Cosmochim. Acta 56, 537–543.

Henehan, M.J., Foster, G.L., Bostock, H.C., Greenop, R., Marshall, B.J., Wilson, P.A., 2016. A new boron isotope-pH calibration for Orbulina universa, with implications for understanding and accounting for 'vital effects'. Earth Planet. Sci. Lett. 454, 282–292.

Henehan, M.J., Rae, J.W.B., Foster, G.L., Erez, J., Prentice, K.C., Kucera, M., Bostock, H.C., Martínez-Botí, M.A., Milton, J.A., Wilson, P.A., Marshall, B.J., Elliott, T., 2013. Calibration of the boron isotope proxy in the planktonic foraminifera Globigerinoides ruber for use in palaeo-CO_2 reconstruction. Earth Planet. Sci. Lett. 364, 111–122.

Herbert, T.D., Lawrence, K.T., Tzanova, A., Peterson, L.C., Caballero-Gill, R., Kelly, C.S., 2016. Late Miocene global cooling and the rise of modern ecosystems. Nat. Geosci. 9, 843.

Heuser, A., Eisenhauer, A., Bohm, F., Wallmann, K., Gussone, N., Pearson, P.N., Nagler, T.F., Dullo, W.C., 2005. Calcium isotope ($\delta^{44/40}$Ca) variations of Neogene planktonic foraminifera. Paleoceanography 20.

Hilgen, F.J., Abels, H.A., Iaccarino, S., Krijgsman, W., Raffi, I., Sprovieri, R., Turco, E., Zachariasse, W.J., 2009. The Global Stratotype Section and Point (GSSP) of the Serravallian Stage (Middle Miocene). Episodes 32, 152–166.

Hönisch, B., Hemming, N.G., Archer, D., Siddall, M., McManus, J.F., 2009. Atmospheric carbon dioxide concentration across the Mid-Pleistocene transition. Science 324, 1551–1554.

Hönisch, B., Ridgwell, A., Schmidt, D.N., Thomas, E., Gibbs, S.J., Sluijs, A., Zeebe, R., Kump, L., Martindale, R.C., Greene, S.E., Kiessling, W., Ries, J., Zachos, J.C., Royer, D.L., Barker, S., Marchitto Jr., T.M., Moyer, R., Pelejero, C., Ziveri, P., Foster, G.L., Williams, B., 2012. The geological record of ocean acidification. Science 335, 1058–1063.

Hoffmann, L.J., Breitbarth, E., Boyd, P.W., Hunter, K.A., 2012. Influence of ocean warming and acidification on trace metal biogeochemistry. Mar. Ecol. Prog. Ser. 470, 191–205.

Hofmann, G.E., Smith, J.E., Johnson, K.S., Send, U., Levin, L.A., Micheli, F., Paytan, A., Price, N.N., Peterson, B., Takeshita, Y., Matson, P.G., Crook, E.D., Kroeker, K.J., Gambi, M.C., Rivest, E.B., Frieder, C.A., Yu, P.C., Martz, T.R., 2011. High-frequency dynamics of ocean pH: a multi-ecosystem comparison. PLoS ONE 6.

Holbourn, A., Kuhnt, W., Frank, M., Haley, B.A., 2013. Changes in Pacific Ocean circulation following the Miocene onset of permanent Antarctic ice cover. Earth Planet. Sci. Lett. 365, 38–50.

Holbourn, A., Kuhnt, W., Simo, J.A., Li, Q.Y., 2004. Middle Miocene isotope stratigraphy and paleoceanographic evolution of the northwest and southwest Australian margins (Wombat Plateau and Great Australian Bight). Palaeogeogr. Palaeoclimatol. Palaeoecol. 208, 1–22.

Horita, J., Zimmermann, H., Holland, H.D., 2002. Chemical evolution of seawater during the Phanerozoic: implications from the record of marine evaporites. Geochim. Cosmochim. Acta 66, 3733–3756.

Hutchins, D.A., Fu, F.X., Zhang, Y., Warner, M.E., Feng, Y., Portune, K., Bernhardt, P.W., Mulholland, M.R., 2007. CO_2 control of Trichodesmium N-2 fixation, photosynthesis, growth rates, and elemental ratios: implications for past, present, and future ocean biogeochemistry. Limnol. Oceanogr. 52, 1293–1304.

IPCC, 2014. Summary for policymakers. In: Field, C.B., et al. (Eds.), Climate Change 2014: Impacts, Adaptation and Vulnerability. Contribution of Working Group II to the Fifth Assessment Report of the Intergovernmental Panel on Climate Change. Cambridge Univ. Press, Cambridge, pp. 1–32.

Keeling, C.D., et al., 2001. In: Ehleringer, J.R., Cerling, T.E., Dearing, M.D. (Eds.), A History of Atmospheric CO_2 and Its Effects on Animals, Plants, and Ecosystems. Scripps Institution of Oceanography. Ch. 5.

Key, R.M., Kozyr, A., Sabine, C.L., Lee, K., Wanninkhof, R., Bullister, J.L., Feely, R.A., Millero, F.J., Mordy, C., Peng, T.H., 2004. A global ocean carbon climatology: results from Global Data Analysis Project (GLODAP). Glob. Biogeochem. Cycles 18.

Klochko, K., Kaufman, A.J., Yao, W., Byrne, R.H., Tossell, J.A., 2006. Experimental measurement of boron isotope fractionation in seawater. Earth Planet. Sci. Lett. 248, 276–285.

Kürschner, W.M., Kvacek, Z., Dilcher, D.L., 2008. The impact of Miocene atmospheric carbon dioxide fluctuations on climate and the evolution of terrestrial ecosystems. Proc. Natl. Acad. Sci. USA 105, 449–453.

LaRiviere, J.P., Ravelo, A.C., Crimmins, A., Dekens, P.S., Ford, H.L., Lyle, M., Wara, M.W., 2012. Late Miocene decoupling of oceanic warmth and atmospheric carbon dioxide forcing. Nature 486, 97–100.

Lear, C.H., Elderfield, H., Wilson, P.A., 2000. Cenozoic deep-sea temperatures and global ice volumes from Mg/Ca in benthic foraminiferal calcite. Science 287, 269–272.

Lear, C.H., Mawbey, E.M., Rosenthal, Y., 2010. Cenozoic benthic foraminiferal Mg/Ca and Li/Ca records: toward unlocking temperatures and saturation states. Paleoceanography 25.

Lear, C.H., Coxall, H.K., Foster, G.L., Lunt, D.J., Mawbey, E.M., Rosenthal, Y., Sosdian, S.M., Thomas, E., Wilson, P.A., 2015. Neogene ice volume and ocean temperatures: insights from infaunal foraminiferal Mg/Ca paleothermometry. Paleoceanography 30, 1437–1454.

Lemarchand, D., Gaillardet, J., Lewin, E., Allegre, C.J., 2002. Boron isotope systematics in large rivers: implications for the marine boron budget and paleo-pH reconstruction over the Cenozoic. Chem. Geol. 190, 123–140.

Le Quere, C., Andrew, R.M., Canadell, J.G., Sitch, S., Korsbakken, J.I., Peters, G.P., Manning, A.C., Boden, T.A., Tans, P.P., Houghton, R.A., Keeling, R.F., Alin, S., Andrews, O.D., Anthoni, P., Barbero, L., Bopp, L., Chevallier, F., Chini, L.P., Ciais, P., Currie, K., Delire, C., Doney, S.C., Friedlingstein, P., Gkritzalis, T., Harris, I., Hauck, J., Haverd, V., Hoppema, M., Goldewijk, K.K., Jain, A.K., Kato, E., Kortzinger, A., Landschutzer, P., Lefevre, N., Lenton, A., Lienert, S., Lombardozzi, D., Melton, J.R., Metzl, N., Millero, F., Monteiro, P.M.S., Munro, D.R., Nabel, J., Nakaoka, S., O'Brien, K., Olsen, A., Omar, A.M., Ono, T., Pierrot, D., Poulter, B., Rodenbeck, C., Salisbury, J., Schuster, U., Schwinger, J., Seferian, R., Skjelvan, I., Stocker, B.D., Sutton, A.J., Takahashi, T., Tian, H.Q., Tilbrook, B., van der Laan-Luijkx, I.T., van der Werf, G.R., Viovy, N., Walker, A.P., Wiltshire, A.J., Zaehle, S., 2016. Global Carbon Budget 2016. Earth Syst. Sci. Data 8, 605–649.

Lisiecki, L.E., Raymo, M.E., 2005. A Pliocene–Pleistocene stack of 57 globally distributed benthic δ^{18}O records. Paleoceanography 20, PA1003. https://doi.org/10.1029/2004PA001071.

Luethi, D., Le Floch, M., Bereiter, B., Blunier, T., Barnola, J.-M., Siegenthaler, U., Raynaud, D., Jouzel, J., Fischer, H., Kawamura, K., Stocker, T.F., 2008. High-resolution carbon dioxide concentration record 650,000–800,000 years before present. Nature 453, 379–382.

Martínez-Botí, M.A., Foster, G.L., Chalk, T.B., Rohling, E.J., Sexton, P.F., Lunt, D.J., Pancost, R.D., Badger, M.P.S., Schmidt, D.N., 2015a. Plio-Pleistocene climate sensitivity evaluated using high-resolution CO_2 records (vol. 518, p. 49, 2015). Nature 526.

Martínez-Botí, M.A., Marino, G., Foster, G.L., Ziveri, P., Henehan, M.J., Rae, J.W.B., Mortyn, P.G., Vance, D., 2015b. Boron isotope evidence for oceanic carbon dioxide leakage during the last deglaciation. Nature 518, 219–222.

Mejía, L.M., Mendez-Vicente, A., Abrevaya, L., Lawrence, K.T., Ladlow, C., Bolton, C.T., Cacho, I., Stoll, H.M., 2017. A diatom record of CO_2 decline since the late Miocene. Earth Planet. Sci. Lett. 479, 18–33.

Myhre, G., Highwood, E.J., Shine, K.P., Stordal, F., 1998. New estimates of radiative forcing due to well mixed greenhouse gases. Geophys. Res. Lett. 25, 2715–2718.

Paelike, H., Lyle, M.W., Nishi, H., Raffi, I., Ridgwell, A., Gamage, K., Klaus, A., Acton, G., Anderson, L., Backman, J., Baldauf, J., Beltran, C., Bohaty, S.M., Bown, P., Busch, W., Channell, J.E.T., Chun, C.O.J., Delaney, M., Dewangan, P., Dunkley Jones, T., Edgar, K.M., Evans, H., Fitch, P., Foster, G.L., Gussone, N., Hasegawa, H., Hathorne, E.C., Hayashi, H., Herrle, J.O., Holbourn, A., Hovan, S., Hyeong, K., Iijima, K., Ito, T., Kamikuri, S.-i., Kimoto, K., Kuroda, J., Leon-Rodriguez, L., Malinverno, A., Moore, T.C. Jr., Murphy, B.H., Murphy, D.P., Nakamura, H., Ogane, K., Ohneiser, C., Richter, C., Robinson, R., Rohling, E.J., Romero, O., Sawada, K., Scher, H., Schneider, L., Sluijs, A., Takata, H., Tian, J., Tsujimoto, A., Wade, B.S., Westerhold, T., Wilkens, R., Williams, T., Wilson, P.A., Yamamoto, S., Yamamoto, Y., Yamazaki, T., Zeebe, R.E., 2012. A Cenozoic record of the equatorial Pacific carbonate compensation depth. Nature 488, 609.

Pagani, M., Arthur, M.A., Freeman, K.H., 1999a. Miocene evolution of atmospheric carbon dioxide. Paleoceanography 14, 273–292.

Pagani, M., Freeman, K.H., Arthur, M.A., 1999b. Late Miocene atmospheric CO_2 concentrations and the expansion of C4 grasses. Science 285, 876–879.

Pagani, M., Zachos, J., Freeman, K.H., Bohaty, S., Tipple, B., 2005. Marked decline in atmospheric carbon dioxide concentrations during the Paleogene. Science 309, 600–603.

Pagani, M., Liu, Z., La Riviera, J., Ravelo, A.C., 2010. High climate sensitivity to atmospheric carbon dioxide for the past 5 million years. Nat. Geosci. 3, 27–30.

Palmer, M.R., Pearson, P.N., Cobb, S.J., 1998. Reconstructing past ocean pH-depth profiles. Science 282, 1468–1471.

Pearson, P.N., 1995. Planktonic foraminifer biostratigraphy and the development of pelagic caps on guyots in the Marshall Islands group. In: Haggerty, J.A., Premoli Silva, I., Rack, F., McNutt, M.K. (Eds.), Proc. ODP, Sci. Results, 144: College Station, TX (Ocean Drilling Program), pp. 21–59.

Pearson, P.N., Chaisson, W.P., 1997. Late Paleocene to middle Miocene planktonic foraminifer biostratigraphy of the Ceara Rise. In: Shackleton, N.J., Curry, W.B., Richter, C., Bralower, T.J. (Eds.), Proc. ODP, Sci. Results, 154: College Station, TX (Ocean Drilling Program), pp. 33–68.

Pearson, P.N., Palmer, M.R., 2000. Atmospheric carbon dioxide concentrations over the past 60 million years. Nature 406, 695–699.

Penman, D.E., Hönisch, B., Rasbury, E.T., Hemming, N.G., Spero, H.J., 2013. Boron, carbon, and oxygen isotopic composition of brachiopod shells: intra-shell variability, controls, and potential as a paleo-pH recorder. Chem. Geol. 340, 32–39.

Penman, D.E., Hönisch, B., Zeebe, R.E., Thomas, E., Zachos, J.C., 2014. Rapid and sustained surface ocean acidification during the Paleocene–Eocene Thermal Maximum. Paleoceanography 29, 357–369.
Perrin, C., 2002. Tertiary: the emergence of modern reef ecosystems. In: Kiessling, W., Flugel, E., Golonka, J. (Eds.), Phanerozoic Reef Patterns. SEPM, Tulsa, pp. 587–621.
Petit, J.R., Jouzel, J., Raynaud, D., Barkov, N.I., Barnola, J.M., Basile, I., Bender, M., Chappellaz, J., Davis, M., Delaygue, G., Delmotte, M., Kotlyakov, V.M., Legrand, M., Lipenkov, V.Y., Lorius, C., Pepin, L., Ritz, C., Saltzman, E., Stievenard, M., 1999. Climate and atmospheric history of the past 420,000 years from the Vostok ice core, Antarctica. Nature 399, 429–436.
Pound, M.J., Haywood, A.M., Salzmann, U., Riding, J.B., Lunt, D.J., Hunter, S.J., 2011. A Tortonian (Late Miocene, 11.61–7.25 Ma) global vegetation reconstruction. Palaeogeogr. Palaeoclimatol. Palaeoecol. 300, 29–45.
Pytkowicz, R.M., Hawley, J.E., 1974. Bicarbonate and carbonate ion-pairs and a model of seawater at 25 °C. Limnol. Oceanogr. 19 (2), 223–234.
Rae, J.W.B., Foster, G.L., Schmidt, D.N., Elliott, T., 2011. Boron isotopes and B/Ca in benthic foraminifera: proxies for the deep ocean carbonate system. Earth Planet. Sci. Lett. 302, 403–413.
Raitzsch, M., Hönisch, B., 2013. Cenozoic boron isotope variations in benthic foraminifers. Geology 41, 591–594.
Raymo, M.E., 1994. The Himalayas, organic carbon burial, and climate in the Miocene. Paleoceanography 9, 399–404.
Raymo, M.E., Ruddiman, W.F., 1992. Tectonic forcing of the late Cenozoic climate. Nature 359, 117–122.
Ridgwell, A., 2005. A Mid Mesozoic Revolution in the regulation of ocean chemistry. Mar. Geol. 217, 339–357.
Ridgwell, A., Zeebe, R.E., 2005. The role of the global carbonate cycle in the regulation and evolution of the Earth system. Earth Planet. Sci. Lett. 234, 299–315.
Sanyal, A., Hemming, N.G., Hanson, G.N., Broecker, W.S., 1995. Evidence for a higher pH in the glacial ocean from boron isotopes. Nature 373, 234–236.
Sanyal, A., Bijma, J., Spero, H., Lea, D.W., 2001. Empirical relationship between pH and the boron isotopic composition of *Globigerinoides sacculifer*: implications for the boron isotope paleo-pH proxy. Paleoceanography 16, 515–519.
Schlitzer, R., 2012. Ocean Data View. http://odv.awi.de.
Seki, O., Foster, G.L., Schmidt, D.N., Mackensen, A., Kawamura, K., Pancost, R.D., 2010. Alkenone and boron-based Pliocene pCO(2) records. Earth Planet. Sci. Lett. 292, 201–211.
Sexton, P.F., Wilson, P.A., Pearson, P.N., 2006. Microstructural and geochemical perspectives on planktic foraminiferal preservation: "Glassy" versus "Frosty". Geochem. Geophys. Geosyst. 7.
Shipboard Scientific Party, 1995. Site 926. In: Curry, W.B., Shackleton, N.J., Richter, C., et al. (Eds.), Proc. ODP, Init. Repts. 154: College Station, TX (Ocean Drilling Program), pp. 153–232.
Shipboard Scientific Party, 1997a. Site 1000. In: Sigurdsson, H., Leckie, R.M., Acton, G.D., et al. (Eds.), Proc. ODP, Init. Repts., 165: College Station, TX (Ocean Drilling Program), pp. 231–289.
Shipboard Scientific Party, 1997b. Site 999. In: Sigurdsson, H., Leckie, R.M., Acton, G.D., et al. (Eds.), Proc. ODP, Init. Repts., 165: College Station, TX (Ocean Drilling Program), pp. 131–230.
Siegenthaler, U., Stocker, T.F., Monnin, E., Luthi, D., Schwander, J., Stauffer, B., Raynaud, D., Barnola, J.M., Fischer, H., Masson-Delmotte, V., Jouzel, J., 2005. Stable carbon cycle-climate relationship during the late Pleistocene. Science 310, 1313–1317.
Sime, N.G., De La Rocha, C.L., Tipper, E.T., Tripati, A., Galy, A., Bickle, M.J., 2007. Interpreting the Ca isotope record of marine biogenic carbonates. Geochim. Cosmochim. Acta 71, 3979–3989.
Spezzaferri, S., Kucera, M., Pearson, P.N., Wade, B.S., Rappo, S., Poole, C.R., Morard, R., Stalder, C., 2015. Fossil and genetic evidence for the polyphyletic nature of the planktonic foraminifera "Globigerinoides", and description of the new genus Trilobatus. PLoS ONE 10.
Spivack, A.J., You, C.F., Smith, H.J., 1993. Foraminiferal boron isotope ratios as a proxy for surface ocean pH over the past 21 Myr. Nature (London) 363, 149–151.
Stap, L.B., de Boer, B., Ziegler, M., Bintanja, R., Lourens, L.J., van de Wal, R.S.W., 2016. CO_2 over the past 5 million years: continuous simulation and new delta B-11-based proxy data. Earth Planet. Sci. Lett. 439, 1–10.
Takahashi, T., Sutherland, S.C., Wanninkhof, R., Sweeney, C., Feely, R.A., Chipman, D.W., Hales, B., Friederich, G., Chavez, F., Sabine, C., Watson, A., Bakker, D.C.E., Schuster, U., Metzl, N., Yoshikawa-Inoue, H., Ishii, M., Midorikawa, T., Nojiri, Y., Koertzinger, A., Steinhoff, T., Hoppema, M., Olafsson, J., Arnarson, T.S., Tilbrook, B., Johannessen, T., Olsen, A., Bellerby, R., Wong, C.S., Delille, B., Bates, N.R., de Baar, H.J.W., 2009. Climatological mean and decadal change in surface ocean pCO(2), and net sea-air CO_2 flux over the global oceans (vol. 56, p. 554, 2009). Deep-Sea Res., Part 1, Oceanogr. Res. Pap. 56, 2075–2076.
Takahashi, T., Sutherland, S.C., Kozyr, A., 2017. Global Ocean Surface Water Partial Pressure of CO_2 Database: Measurements Performed During 1957–2016 (LDEO Database Version 2016) (NCEI Accession 0160492). Version 3.3. NOAA National Centers for Environmental Information Dataset.
Tyrrell, T., Zeebe, R.E., 2004. History of carbonate ion concentration over the last 100 million years. Geochim. Cosmochim. Acta 68, 3521–3530.
Vengosh, A., Kolodny, Y., Starinsky, A., Chivas, A.R., McCulloch, M.T., 1991. Coprecipitation and isotopic fractionation of boron in modern biogenic carbonates. Geochim. Cosmochim. Acta 55, 2901–2910.
Warren, A., Bottier, D.J., 2001. Evolutionary Paleoecology: The Ecological Context of Macroevolutionary Change. Columbia University Press.
Wilson, M.E.J., 2008. Global and regional influences on equatorial shallow-marine carbonates during the Cenozoic. Palaeogeogr. Palaeoclimatol. Palaeoecol. 265, 262–274. https://doi.org/10.1016/j.palaeo.2008.05.012.
Winkelmann, Levermann, A., Ridgwell, A., Caldeira, K., 2015. Combustion of available fossil-fuel resources sufficient to eliminate the Antarctic Ice Sheet. Sci. Adv. 1, e1500589.
Zachos, J., Pagani, M., Sloan, L., Thomas, E., Billups, K., 2001. Trends, rhythms, and aberrations in global climate 65 Ma to present. Science 292, 686–693.
Zachos, J.C., Dickens, G.R., Zeebe, R.E., 2008. An early Cenozoic perspective on greenhouse warming and carbon-cycle dynamics. Nature 451. https://doi.org/10.1038/nature. 17 January 2008.
Zeebe, R.E., 2012. History of seawater carbonate chemistry, atmospheric CO_2, and ocean acidification. Annu. Rev. Earth Planet. Sci. 40 (40), 141–165.
Zhang, Y.G., Pagani, M., Liu, Z., Bohaty, S.M., DeConto, R., 2013. A 40-million-year history of atmospheric CO_2. Philos. Trans. R. Soc. A, Math. Phys. Eng. Sci. 371.
Zhang, Y.G., Pagani, M., Liu, Z.H., 2014. A 12-million-year temperature history of the tropical Pacific Ocean. Science 344, 84–87.